Complex conductivity of tight sandstones

André Revil, Antoine Coperey, Yaping Deng, Adrian Cerepi, Nikita Seleznev

HAL Id: hal-02324287
https://hal.science/hal-02324287

Submitted on 23 Nov 2020

Complex conductivity of tight sandstones

André Revil[1], Antoine Coperey[1], Yaping Deng[2], Adrian Cerepi[3], and Nikita Seleznev[4]

ABSTRACT

Induced polarization well logging can be used to characterize sedimentary formations and their petrophysical properties of interest. That said, nothing is really known regarding the complex conductivity of low-porosity sedimentary rocks. To fill this gap of knowledge, we investigate the complex conductivity of 19 tight sandstones, one bioclastic turbidite, and four sand/smectite mixes. The sandstones and the bioclastic turbidite are characterized by low to very low porosities (in the range of 0.8%–12.3%) and a relatively narrow range of cation exchange capacity (CEC — 5–15 meq/100 g). The sand-clay mixtures are prepared with pure smectite (Na-Montmorillonite, porosity approximately 90%, CEC 75 meq/100 g) and a coarse sand (grain size approximately 500 µm). Data quality is assessed by checking that the percentage frequency effect between two frequencies separated by a decade is proportional to the value of the phase lag measured at the geometric frequency. We also checked that the normalized chargeability determined between two frequencies is proportional to the quadrature conductivity at the geometric mean frequency. Our experimental results indicate that the surface conductivity, the normalized chargeability, and the quadrature conductivity are highly correlated to the ratio between the CEC and the bulk tortuosity of the pore space. This tortuosity is obtained as the product of the (intrinsic) formation factor with the (connected) porosity. The quadrature conductivity is proportional to the surface conductivity. All these observations are consistent with the predictions of the dynamic Stern layer model, which can be used to assess the magnitude of the polarization associated with these porous media over the full range of porosity. The next step will be to extend and assess this model to partially saturated sandstones.

INTRODUCTION

Complex conductivity refers to the study of electromigration and local charge storage in porous media. It corresponds to a set of material properties determined in a geophysical method known as induced polarization (Schlumberger, 1920). The in-phase component (the real part of the complex conductivity) refers to pure electromigration processes (Waxman and Smits, 1968), i.e., the migration, in a solvent, of the charge carriers under the influence of an external (applied) electrical field. The quadrature component (imaginary part of the complex conductivity) refers to reversible charge accumulations at some polarization length scales corresponding to grains or pores (Vinegar and Waxman, 1984). Such low-frequency polarization is associated with charge migration/diffusion under the influence of a gradient in the chemical potential of the charge carriers in the solvent (Fixman, 1980; Grosse and Shilov, 2000; Grosse, 2009). In absence of metallic particles, the ability of a porous material to store reversibly electrical charges can be also described by a normalized chargeability corresponding to the product of the chargeability by the (high-frequency) electrical conductivity of the material (e.g., Mansoor and Slater, 2007). This normalized chargeability is directly proportional to the cation exchange capacity (CEC) and therefore, in first approximation, to the clay-mineral content of the rocks when the clay mineralogy remains constant (for volcanic rocks, see Revil et al., 2017a, 2017b).

Vinegar and Waxman (1984) are probably the first to recognize that two concurrent electrochemical polarization mechanisms may explain the low-frequency (<10 kHz) polarization of porous rocks. The first is related to the polarization of the electrical double layer (DL) surrounding the grains, i.e., to charge accumulation and diffusion of the counterions in the Stern and diffuse layers. Leroy et al. (2008) emphasize the role of the inner portion of the electrical DL, called the Stern layer, in the polarization of porous media (see also Chelidze and Guéguen, 1999). The second low-frequency polarization mechanism is called membrane polarization (e.g., Marshall and Madden, 1959; Titov et al., 2010; Bücker and Hördt, 2013a, 2013b). The mechanism is due to the gradient in the Hittorf numbers of the ions through the pore network, which in turn generates charge concentration gradients under the application of a primary electrical field or electrical current. These Hittorf numbers correspond to the fraction of current carried by a given type of ion and are influenced by the CEC of the material (e.g., Revil, 1999). Therefore, the gradient in the Hittorf numbers is controlled by the variations in the CEC of the material. Following these ideas, Vinegar and Waxman (1984) hypothesize that the surface conductivity and the quadrature conductivity would be influenced by the CEC of the material.

The dynamic Stern layer model developed later by Revil and Florsch (2010) and Revil (2012, 2013a, 2013b) has shown some promises in explaining all the aspects of complex conductivity of porous media without the need for membrane polarization. It is based on the tangential mobility of the counterions (forming outer sphere complexes in the Stern layer) along the mineral/water inter-

Figure 1. Relationship between SSA and CEC for clay minerals and clay-rich porous materials. SSA as a function of CEC (in meq g^{-1} with $1 \text{ meq g}^{-1} = 96{,}320 \text{ C kg}^{-1}$ in SI units). The two lines correspond to a surface charge density of one to three elementary charges per unit surface area. Modified from Revil et al. (2013a, 2013b). Therefore, data show that the average surface charge density is approximately two elementary charges per nm^2 ($Q_S = 0.32 \text{ Cm}^{-2}$).

face. This concept was developed in colloidal chemistry by Zukoski and Saville (1986a, 1986b) and Rosen and Saville (1991). It is assumed that the polarization of the Stern layer is the dominating mechanism and that membrane polarization is vanishingly small or occurs at very low frequencies (<10 mHz, see Leroy and Revil, 2009). It also explains the observations made by Vinegar and Waxman (1984) regarding the influence of the bulk tortuosity with respect to the quadrature conductivity.

Currently, the dynamic Stern layer model is further tested to check its heuristic predictions to a broader class of porous media, including volcanic rocks (Revil et al., 2017a, 2017b), oil and gas shales (Revil et al., 2013a, 2013b; Woodruff et al., 2014), and soils (Revil et al., 2017c). Very few studies (e.g., Zisser and Nover, 2009; Zisser et al., 2010) have been performed on low-porosity (tight) sandstones, which is the subject of the present investigation. These published works were related to the connection between permeability and the main relaxation time of these materials and not in explaining the magnitude of the induced polarization in terms of a physics-based model. Induced polarization can be used to assess oil saturation in oil and gas tight reservoirs by analyzing well-log data (either the conductivity and the phase or the dispersion of the conductivity with the frequency). Various papers have shown how complex conductivity can be very useful to estimate oil and gas saturations in siliciclastic materials (Olhoeft, 1985, Kemna et al., 2004, Davydycheva et al., 2006; Schmutz et al., 2010, 2012).

In the present paper, we are mostly interested to test the dynamic Stern layer model of polarization to a new set of 20 saturated consolidated low-porosity (<12%) sedimentary core samples (19 tight sandstones and 1 bioclastic turbidite). These core samples were extracted from an Eocene fluvial-dominated deltaic formation. We performed complex conductivity measurements at three salinities (approximately at 0.1, 1, and 10 S m^{-1} NaCl brine, 25°C). To contrast these samples, we also performed measurements with four samples made using a clean sand and a smectite. For these clay/quartz samples, the samples are Sd100: 100% quartz, Sd95: 5% smectite/95% quartz, Sd90: 10% smectite/90% quartz, and S100: 100% smectite sample (% in weight fraction of solid matrix grains). In principle, the dynamic Stern layer model should be able to explain all the spectra with the same values of the fundamental parameters used in the model whatever the porosity. These are the key scientific questions we want to address: (1) How predictive is the Stern layer model for these materials? (2) What are the dependences of the surface conductivity, quadrature conductivity, and normalized chargeability with the CEC and with the tortuosity of the bulk pore space? (3) Is the ratio of quadrature conductivity to surface conductivity consistent with other sedimentary materials and volcanic rocks? We will also take advantage of the present study to reassess the value of the mobility of the counterions in the Stern and diffuse layers. A future work will focus on the relationship between the complex conductivity spectra of tight sandstones and the saturation and permeability.

THEORY

All porous media investigated in the present study have in common the existence of an electrical DL coating the surface of the mineral grains. The electrical DL is formed by the combination of the Stern and diffuse layers (e.g., Gouy, 1910; Rosen and Saville, 1991). Usually, because of their high specific surface area (SSA), the exposed interface between the minerals and the pore water is
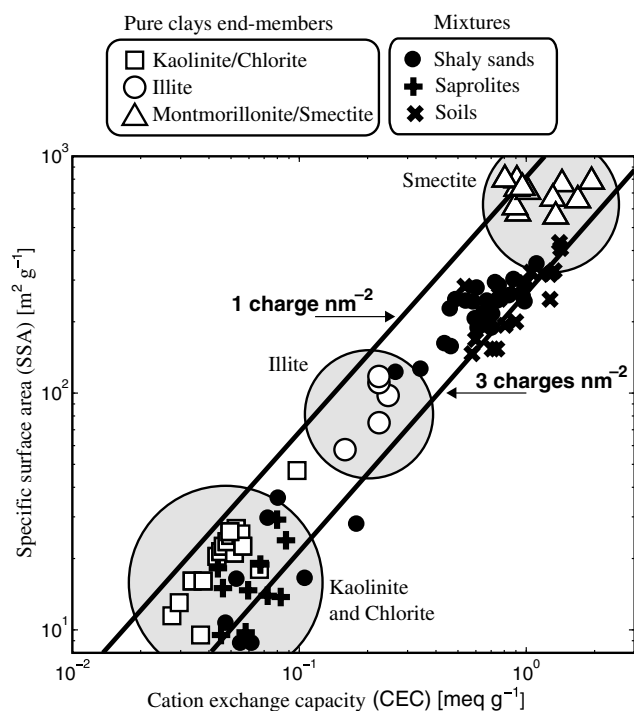
dominated by the presence of clay minerals. Figures 1 and 2 show the relationship between the SSA (symbol S_{Sp}) and the CEC for clayey materials and pure clay minerals (including our data set, which we will come back to later). The ratio between the CEC and S_{Sp} denotes the charge per unit surface area, which is typically two to five elementary charges per nm^2. The conduction and low-frequency polarization of a porous material with silicates and aluminosilicates, such as those used in the present study, is due to the conduction and polarization of this electrical DL and the adjacent pore water (Figure 3a). These properties are therefore strongly influenced by the CEC or alternatively by S_{Sp}. For instance, for a soil containing a mineral such as smectite (characterized by a high CEC and S_{Sp}), the conductivity associated with conduction in the electrical DL and the polarization of the sandstones and clay-sand mixes is expected to be very strong by comparison with a material characterized by a low clay content. We will check in the present work that smectite has indeed the highest surface conductivity and quadrature conductivity among clay minerals and porous media. Our goal is also to show that the dynamic Stern layer model works for a broad class of porous media, including very high and low-porosity materials.

Complex conductivity for the dynamic Stern layer model

According to the dynamic Stern layer model and using harmonic current excitations behaving as $E = E_0 \exp(+i\omega t)$, the complex conductivity of a water-saturated porous material is given by (e.g., Revil et al, 2013a, 2013b, 2017b)

$$\sigma^*(\omega) = \sigma_\infty \left(1 - M \int_0^\infty \frac{h(\tau)}{1 + (i\omega\tau)^{1/2}} d\tau \right) + i\omega\varepsilon_\infty, \quad (1)$$

where ω denotes the angular frequency (rad s^{-1}), $\varepsilon_\infty (> 0)$ denotes the high-frequency permittivity (in $F\,m^{-1} = A\,s\,V^{-1}\,m^{-1}$ actually the low-frequency part of the Maxwell Wagner polarization or the high-frequency dielectric permittivity in the absence of Maxwell Wagner polarization), τ is a time constant (also called the relaxation time because it is corresponding to a diffusion process), $h(\tau)$ denotes the (normalized) probability density associated with the distribution of the time constants of the material (in turn related to its distribution of polarization length scales), $M = (\sigma_\infty - \sigma_0)/\sigma_\infty$ is the dimensionless chargeability, and σ_0 and σ_∞ denote the direct current (DC, $\omega = 0$) and high-frequency electrical conductivities (in $S\,m^{-1} = A\,V^{-1}\,m^{-1}$), respectively.

Usually, we also define a normalized chargeability as $M_n = M\sigma_\infty = \sigma_\infty - \sigma_0$, which is expressed in $S\,m^{-1}$. This normalized chargeability is introduced because, according to the dynamic Stern layer model, it is proportional to the CEC of the material (e.g., Mao et al., 2016). We will investigate the validity of this claim for tight sandstones in this paper for which independent CEC measurements will be obtained. Equation 1 can eventually simplify to a Cole-Cole model for complex conductivity (Cole and Cole, 1941), which is distinct from the Cole-Cole model developed by Pelton et al. (1978) for complex resistivity (see a detailed discussion in Tarasov and Titov, 2013). In equation 1, the function $[1 + (i\omega\tau)^{1/2}]^{-1}$ is called the kernel and corresponds here to a Warburg decomposition for the reason described in detail in several of our previous papers (see discussions in Revil et al., 2014a; Niu and Revil, 2016). Finally, the relaxation time distribution $h(\tau)$ in equation 1 is a normalized probability den-

sity function related to the pore-size or grain-size distributions (e.g., Revil and Florsch, 2010; Revil et al., 2014a).

The high- and low-frequency conductivities can be obtained through a volume averaging method (see Cole-Cole model derivation in Revil, 2013a, 2013b) in the so-called linear conductivity model:

$$\sigma_0 = \frac{1}{F}\sigma_w + \left(\frac{1}{F\phi}\right)\rho_g\beta_{(+)}(1 - f)\text{CEC}, \quad (2)$$

$$\sigma_\infty = \frac{1}{F}\sigma_w + \left(\frac{1}{F\phi}\right)\rho_g[\beta_{(+)}(1 - f) + \beta_{(+)}^S f]\text{CEC}, \quad (3)$$

where F (dimensionless) denotes the intrinsic formation factor related to the porosity ϕ (dimensionless) by Archie's (1942) law $F = \phi^{-m}$ ($m \geq 1.0$ is called the cementation or porosity exponent), σ_w (in $S\,m^{-1}$) denotes the pore-water conductivity, f (dimensionless) denotes the partition coefficient for the counterions between the diffuse and the Stern layers (i.e., the fraction of counterions in the Stern layer), ρ_g is the grain density (in $kg\,m^{-3}$, typically $\rho_g = 2700$ $kg\,m^{-3}$ for the rocks investigated in the present study), and CEC is the cation exchange capacity of the material (usually reported in meq/100 g but expressed in $C\,kg^{-1}$ in the international system of units, 1 meq/(100 g) = 963.2 $C\,kg^{-1}$). The values of the mobility of ions in diffuse layer of sedimentary rocks are the same as in the bulk pore water with $\beta_{(+)}(Na^+, 25°C) = 5.2 \times 10^{-8}$ $m^2\,s^{-1}\,V^{-1}$. The value of the mobility of the counterions in the Stern layer $\beta_{(+)}^S$ will be discussed in detail below.
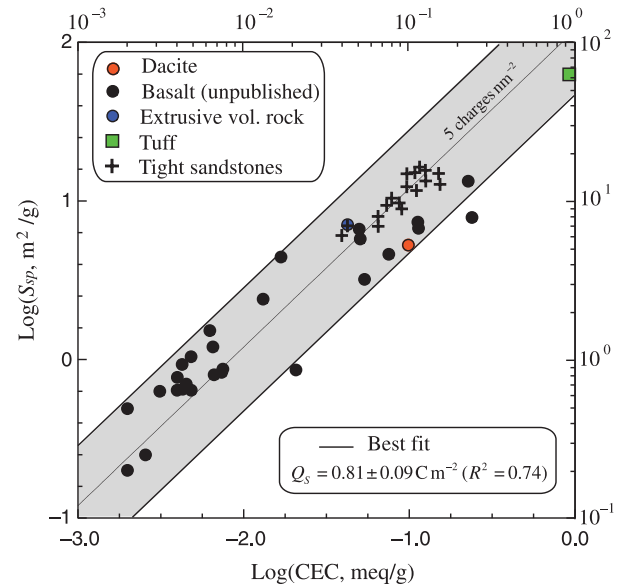

Figure 2. The SSA versus CEC for the sandstones used in the present study (tight sandstones) and volcanic rocks (1 meq = 96.32 C). The linear trend (in a log-log plot) is used to determine the average surface charge density of the mineral surface, which is approximately five elementary charges per nm^2 ($Q_S = 0.81 \pm 0.08$ Cm^{-2}). The dacite data (CEC = 0.10 meq g^{-1}, SSA 6.4 $m^2\,g^{-1}$) are from Shinzato et al. (2012) (CEC obtained with the NH_4-Na titration method). The data for the extrusive volcanic rock (CEC = 0.0404 meq g^{-1}, SSA 7.0 $m^2\,g^{-1}$) are from Lira et al. (2013), CEC measured with the ammonium acetate method and SSA with the BET method). The tuff data (CEC = 0.98 meq g^{-1}, SSA 63.0 $m^2\,g^{-1}$) are from Godelitsas et al. (2010).

Surface conductivity and normalized chargeability

Equations 2 and 3 can be written as a linear model for the conductivity (i.e., the conductivity of the sample depends linearly on the conductivity of the brine)

$$\sigma' = \frac{1}{F}\sigma_w(1 + F\mathrm{Du}), \qquad (4)$$

$$\sigma' = \frac{1}{F}\sigma_w + \sigma_S, \qquad (5)$$

where σ_S (in S m^{-1}) denotes the surface conductivity of the material and $\mathrm{Du} = \sigma_S/\sigma_w$ denotes the dimensionless Dukhin number (Dukhin and Shilov, 1974). Equation 5 connects the conductivity, the conductivity of the pore water σ_w, and the surface conductivity σ_S (see Figure 3).

The (high-frequency) surface conductivity (see the discussion in Appendix A) and the normalized chargeability are given by (Revil, 2013a, 2013b)
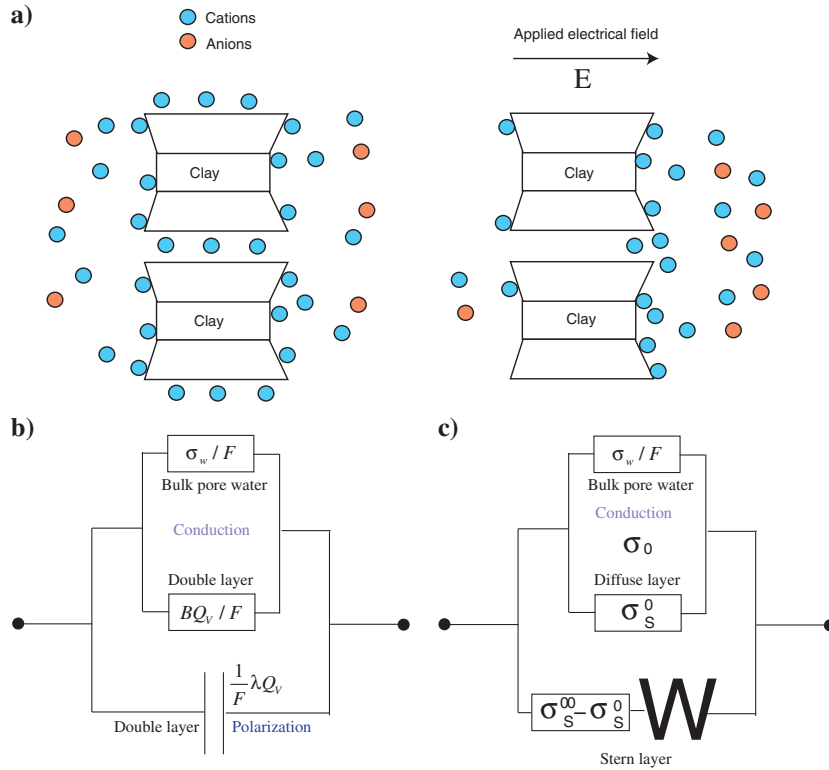
Figure 3. Polarization of clayey materials. (a) Sketch of the polarization of a clay grain. In equilibrium, there is an excess of cations (in blue) associated with the clay grains in the diffuse layer associated with the basal planes and the amphoteric sites covering the edges of the clay crystal and the Stern layer on the edges. In the presence of an electrical field **E**, the clay particles get polarized due to the electromigration of the cations in the direction of the electrical field (Stern layer polarization) and the formation of a salinity gradient on each side of the grain (membrane polarization). This polarization provides a dipole moment to the clay particles. (b) First-order approximation of the equivalent circuit of a clayey rock according to Vinegar and Waxman (1984). Conduction comprises two contributions, one associated with the bulk pore water and the other with conduction in the electrical DL (surface conductivity). The capacitance corresponds to the polarization of the electrical DL coating the surface of the grains. (c) Equivalent circuit of a clayey rock according to the dynamic Stern layer model. The W denotes a Warburg-type capacitance.

$$\sigma_S = \left(\frac{1}{F\phi}\right)\rho_g[\beta_{(+)}(1 - f) + \beta_{(+)}^S f]\mathrm{CEC}, \qquad (6)$$

$$M_n = \left(\frac{1}{F\phi}\right)\rho_g\beta_{(+)}^S f\mathrm{CEC}. \qquad (7)$$

A more refined model of frequency-dependent surface conductivity is discussed in Appendix A. This model explains the difference between the Vinegar and Waxman (1984) model (see Figure 3b) and the dynamic Stern layer model (shown in Figure 3c). In our model, the Stern layer contribution is the source for the frequency-dependent surface conductivity, whereas the model of Vinegar and Waxman (1984) does not account for such frequency dependence. Note that in equations 6 and 7, the surface conductivity and the normalized chargeability are inversely proportional to the product $F\phi$, which corresponds to the tortuosity of the pore space. This is a fundamental consequence of the dynamic Stern layer model that is not explained by alternative models, such as the membrane polarization model or the model proposed initially by Vinegar and Waxman (1984). Equation 6 can be also written as $\sigma_S = \rho_g B(\mathrm{CEC}/F\phi)$, where $B \equiv \beta_{(+)}(1 - f) + \beta_{(+)}^S f$ corresponds to an apparent mobility for surface conduction as in the empirical model proposed in the seminal paper of Waxman and Smits (1968).

The charge density per unit surface area (in C m^{-2}) Q_S denotes the available charge density of counterions that can be sorbed on the mineral surface. It is therefore defined as the ratio of the CEC by the SSA of the material S_{Sp} (in m^2 kg^{-1})

$$Q_S = \frac{\mathrm{CEC}}{S_{Sp}}. \qquad (8)$$

The SSA can be measured by the so-called *BET technique* using nitrogen adsorption (see the details in Lowell and Shields, 1979). For clay minerals, the mean charge density Q_S is typically two elementary charges per nm^2 ($Q_S = 0.32$ C m^{-2}; see Figure 1). This charge density is an average of the volumetric charge density related to the isomorphic substitutions and the charge associated with the amphoteric sites on the edge of the clay crystals. From equations 6–8, we can write the surface conductivity and the normalized chargeability as a function of the SSA

$$\sigma_S = \left(\frac{1}{F\phi}\right)\rho_g[\beta_{(+)}(1 - f) + \beta_{(+)}^S f]Q_S S_{Sp}, \qquad (9)$$

$$M_n = \left(\frac{1}{F\phi}\right)\rho_g\beta_{(+)}^S f Q_S S_{Sp}. \qquad (10)$$

These equations show that the surface conductivity and the normalized chargeability (therefore the quadrature conductivity) are proportional to

the SSA in addition to being controlled by the (bulk) tortuosity of the bulk pore space $F\phi$.

Two other quantities of interest are the charge per unit pore volume (used instead of the CEC, i.e., the charge per unit mass of grains) and the surface per pore volume ratio (used instead of the SSA, i.e., a surface per unit mass of grains). These parameters are defined by

$$Q_V = \rho_g \left(\frac{1 - \phi}{\phi} \right) \text{CEC}, \tag{11}$$

$$S_{\text{por}} = \frac{S}{V_p} = \rho_g \left(\frac{1 - \phi}{\phi} \right) S_{Sp}, \tag{12}$$

respectively. The inverse of S_{por} corresponds to a hydraulic radius (i.e., for a capillary, it would be exactly the radius of the capillary). As shown by Revil (2013a, 2013b), these two parameters can be used to determine the surface conductivity and normalized chargeability

$$\sigma_S = \frac{1}{F} B Q_V, \tag{13}$$

$$M_n = \frac{1}{F} \lambda Q_V, \tag{14}$$

with $B \equiv \beta_{(+)}(1 - f) + \beta_{(+)}^S f$ being an apparent mobility for surface conduction (and similarly $\lambda = \beta_{(+)}^S f$ for the quadrature conductivity). The equivalent linear circuit of a sandstone described by such a model is sketched as in Figure 3b and can be seen as two resistances in parallel to a capacitance. This is, however, a very simplistic view of the problem because in this approach (corresponding to the Vinegar and Waxman model), the conductivity itself is independent of the frequency (in contrast to the model shown in Figure 3c). Because the surface charge density is related to the volumetric charge density by $Q_S = Q_V V_p / S$, we have

$$\sigma_S = \frac{1}{F} B Q_S S_{\text{por}}, \tag{15}$$

$$M_n = \frac{1}{F} \lambda Q_S S_{\text{por}}, \tag{16}$$

(and similarly for the quadrature conductivity). Equation 15 is similar to the equations developed empirically by Waxman and Smits (1968) and Cremers (1968). An equation similar to equation 16 for the quadrature conductivity can also be found in Vinegar and Waxman (1984). Equations 15 and 16 are also similar to the equations developed by Börner (1991, 1992) for the surface conductivity and the quadrature conductivity.

The surface conductivity is inherently difficult to measure in the laboratory because the linear conductivity model described above is only valid when the surface conductivity is small. When the surface conductivity is high, this high-salinity assumption is not valid anymore and the relationship between the conductivity of the porous material and the pore-water conductivity is becoming nonlinear. The normalized chargeability may also be difficult to accurately measure because it requires very broadband measurements. In time-domain induced polarization, the normalized chargeability can be measured, but this requires that all the polarization-length scales have been fully polarized, which can be achieved only through a long duration (100–200 s) of the primary current injection.

Quadrature conductivity

The quadrature conductivity is easily measurable, but its value is frequency dependent. In addition, at high frequencies, >1 kHz, the quadrature conductivity associated with the polarization of the DL of the grains can be masked by the Maxwell Wagner polarization and true dielectric effects. Following our previous paper (e.g., Revil et al., 2015), we can define a linear relationship between the quadrature conductivity and the normalized chargeability

$$\sigma'' \approx -\frac{M_n}{\alpha} - \omega \varepsilon_\infty, \tag{17}$$

where α has been taken equal to 1 or 5 in Revil et al. (2015). The value of α will be determined using equations determined from the Drake's model, also called the *constant-phase model*. Following Revil et al. (2015) and for frequencies for which the dielectric term $-\omega \varepsilon_\infty$ is negligible in equation 17, we use the following definition for the dimensionless number R:

$$R \equiv \frac{M_n}{\sigma_S} \approx -\alpha \left(\frac{\sigma''}{\sigma_S} \right), \tag{18}$$

and $-\sigma''/\sigma_S = R/\alpha$. Using equations 6 and 7, or alternatively equations 15 and 16, this dimensionless number R can be related to the partition coefficient f of the counterions between the Stern and diffuse layers (Revil et al., 2015) by

$$R = \frac{\beta_{(+)}^S f}{[\beta_{(+)}(1 - f) + \beta_{(+)}^S f]} = \frac{\lambda}{B}. \tag{19}$$

We will investigate below the value of this dimensionless number for our new data set, and we will estimate the value of the mobility of the counterions in the Stern layer $\beta_{(+)}^S$ as well as the value of the partition coefficient f.

Extension to unsaturated conditions

Although the extension of our model is not explored further in unsaturated conditions, it may be worth expending quickly the simplified model described above for such case. Extending the models of Waxman and Smits (1968) and Vinegar and Waxman (1984) to unsaturated conditions yields

$$\sigma'(s_w) = \frac{1}{F} s_w^n \sigma_w + s_w^{n-1} \left(\frac{1}{F\phi} \right) \rho_g [\beta_{(+)}(1 - f) + \beta_{(+)}^S f] \text{CEC},$$

$$\tag{20}$$

$$\sigma''(s_w) = - \left(\frac{1}{F\phi} \right) s_w^{n-1} \frac{\lambda}{\alpha} \rho_g \text{CEC}, \tag{21}$$

$$M_n(s_w) = \left(\frac{1}{F\phi} \right) s_w^{n-1} \lambda \rho_g \text{CEC}, \tag{22}$$

Sample 3

Sample 4
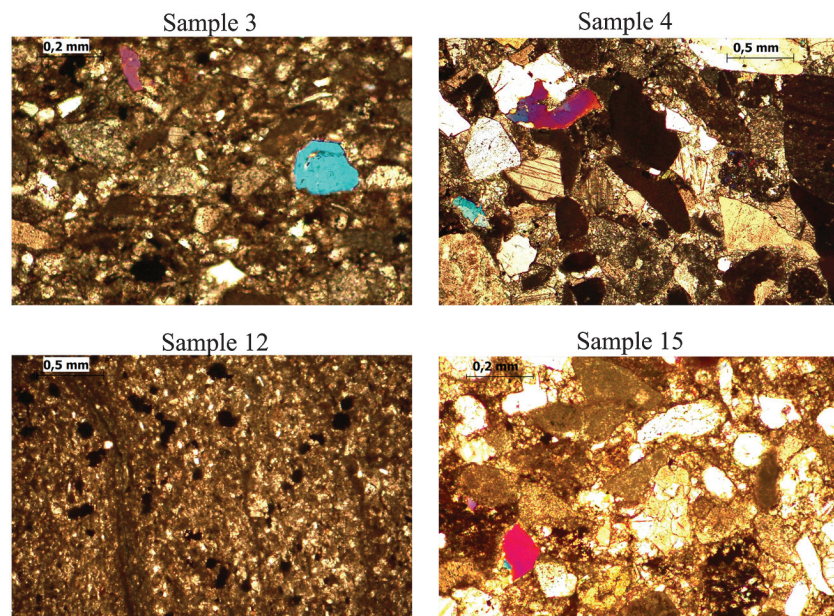

Sample 12

Sample 15

Figure 4. Thin sections of four characteristic tight sandstones. The size of the grains differs strongly from one sample to the other. The grain-size distribution is expected to be quite broad explaining in turn the potential broad range of the relaxation times for the core samples. The clay fraction of these samples is dominated by illite.

Table 1. Mineralogy (from transmission FTIR, Fourier transform infrared spectroscopy; all data are expressed in wt%).[5]

Name	Q	F	Na-P	C	D	A	I	S	K	C	M	P
20161501	20	0	0	34	6	2	19	6	1	5	8	1
20161502	18	2	0	43	5	1	20	5	0	2	2	2
20161503	15	2	0	59	4	0	12	4	0	1	1	1
20161504	15	6	4	67	2	0	2	2	0	0	0	1
20161505	9	1	0	56	6	2	14	4	0	5	3	0
20161506	7	1	0	45	15	3	15	4	1	5	5	1
20161507	16	5	3	56	4	1	9	3	0	3	1	1
20161508	15	1	0	76	0	0	2	2	0	2	1	0
20161509	26	2	0	29	8	0	24	6	0	2	1	2
20161510	19	1	0	61	2	1	9	3	0	2	2	1
20161511	13	1	0	68	0	0	11	4	0	0	0	3
20161512	14	4	3	48	16	0	7	4	0	3	1	1
20161513	19	5	3	59	5	0	4	2	0	1	0	1
20161514	13	4	1	66	3	0	10	3	0	1	0	1
20161515	14	2	0	56	1	0	18	5	0	2	2	2
20161516	17.	7	4	56	6	0	6	3	0	1	0	1
20161517	17	8	5	62	2	0	4	2	0	0	0	0
20161518	17	4	1	56	10	0	7	3	0	0	0	2
20161519	12	2	0	63	1	1	12	4	0	3	1	1
20161520	14	2	0	59	1	0	16	5	0	2	1	1

[5]Q, Quartz; F, K-Feldspar; Na-P, Na-plagioclase; C, calcite; D, dolomite; A, ankerite; I, illite; S, smectite; K, kaolinite; C, chlorite; M, muscovite; and P, pyrite. We see that the two main minerals are calcite and quartz and that the clay fraction is dominated by illite.

where s_w ($0 \leq s_w \leq 1$) denotes the saturation and $n > 1$ is the second Archie's exponent (saturation exponent).

MATERIAL AND METHODS

Samples

Twenty core samples were extracted from an Eocene fluvial-dominated deltaic formation, including 19 sandstones per se and one bioclastic turbidite (sample #20). Some thin sections are shown in Figure 4. The thin sections show that the core samples exhibit very distinct microstructures. The mineralogy of the 20 core samples is provided in Table 1. The composition of these rocks, besides quartz, clays, and feldspars, includes a significant fraction of carbonate lithic fragments and some small amount of pyrite. In some samples, the fraction of carbonate can be up to 76%. A picture of the 20 core samples with the impedance meter is shown in Figure 5. We can see that some of the core samples exhibit some damage with the presence of cracks. The axis of symmetry of the cylindrical core samples is perpendicular to the axis of symmetry of the borehole. The axis of symmetry is parallel to the bedding, and therefore the four-electrode measurement method, applied along the symmetry axis of the core samples, probes the horizontal conductivity.

For the sand-clay mixtures, the clean sand is a well-sorted sand with a grain size in the range of $500 - 600 \, \mu m$. The smectite corresponds to the SWy-2-smectite from the Clay Mineral Society. It is a Na-Montmorillonite from the Cretaceous Newcastle Formation (Wyoming, USA). Its measured CEC (using the ammonium displacement method) is 75 meq/100 g. For the Sd95 mixture, the clay particles filled half of the pore space between the sand grains, whereas for the Sd90 mixture, the clay particles filled all the space between the sand grains (Appendix B). This is due to the very high porosity of the smectite (approximately 90%).

Experimental setup

To prevent electrical leakages and drying of the sandstone core samples, we use an insulating tape around the external side of the core samples (Figure 6). The samples are connected to the ZEL-SIP04-V02 impedance meter using two voltage electrodes M and N and two current electrodes A and B (Figure 6). Two electrodes are used at the end faces as current electrodes A and B (Figure 6). Two other electrodes are used on the side as voltage electrodes (M and N). A spring was used to push the current electrodes against the core sample, always having the same

uniaxial pressure. Great care was taken to have no surface of the core samples exposed to air during the measurements to avoid their drying. The electrodes are also in direct contact with the core sample to avoid water-filled spaces between them that could create spurious resistances that are expected to vary with the salinity as in the experimental setup proposed, for instance, by Vinegar and Waxman (1984). We performed different preliminary tests to choose the most suitable electrodes for the current and voltage electrodes. The geometric factor is determined as $g = L/A$, where L is the separation between the two voltage electrodes and A denotes the surface area of a cross section of the core sample. The result is close to $17.7 m^{-1}$, which has been checked using a numerical test using a finite-element solver.

For the first experiment (done with the lowest salinity), the core samples have been gently dried in an oven and then fully saturated under vacuum conditions. The solutions used for the saturations are NaCl solutions that have been first degassed. Salt solutions were made up by weight through the addition of dry NaCl salt (from Labosi, Fisher Scientific, ref. A4890853, 99% pure) to a certain volume of demineralized water. The electrical conductivity of the NaCl solutions $\sigma_w(C_f; T)$ is determined from the salinity and the temperature according to the formula proposed by Sen and Goode (1992). Electrical conductivity measurements were checked with a calibrated conductimeter (Fisher AB200 pH/conductivity meter). The final solutions at equilibrium can be slightly different at the two lowest salinities (typically the conductivity at equilibrium is $0.10 - 0.16 \, S\,m^{-1}$) possibly due to the dissolution of carbonate into the first solution.

For the soft-core samples, we used a different setup, which is similar to the setup used recently in Revil et al. (2017c). We keep the samples in buckets covered with a 3D printed cap to avoid desaturation during the course of the experiments (Figure 7). Four equally spaced nonpolarizing Ag-AgCl$_2$ sintered electrodes (diameter 4×1 mm) are placed in the top of the bucket with a cap. The distance between the electrodes is 2 cm, the height of the bucket is 2.5 cm, and its diameter is 7.0 cm (Figure 7). Such types of electrode configuration have been used before for spectral-induced polarization measurements (e.g., Van Voorhis et al., 1973; Schmutz et al., 2010; Vaudelet et al., 2011a, 2011b), and benchmarks of these electrode configurations can be found in those papers. This type of electrodes configuration is very similar to the ones used in field conditions (Wenner-α type array). It avoids issues with the approach used in Vinegar and Waxman (1984), such as the need for computing the resistances due to the water-filled reservoirs between the electrodes and the core sample. Also, the current lines do not need to be homogeneous through the core sample and, as shown by Vaudelet et al. (2011a, 2011b), the sensitivity map can be plotted for any electrode configurations taking into account the electrode configuration, the size of the electrodes, and the boundary conditions applied to the sample (insulating boundaries outside the position of the electrodes themselves).

For the first experiment (i.e., performed at the lowest salinity), the samples were first dried and then saturated under vacuum with a degassed solution. For this sample holder, we use two distinct procedures to get the geometric factor. The first procedure is based on using Comsol Multiphysics to numerically solve Laplace equation
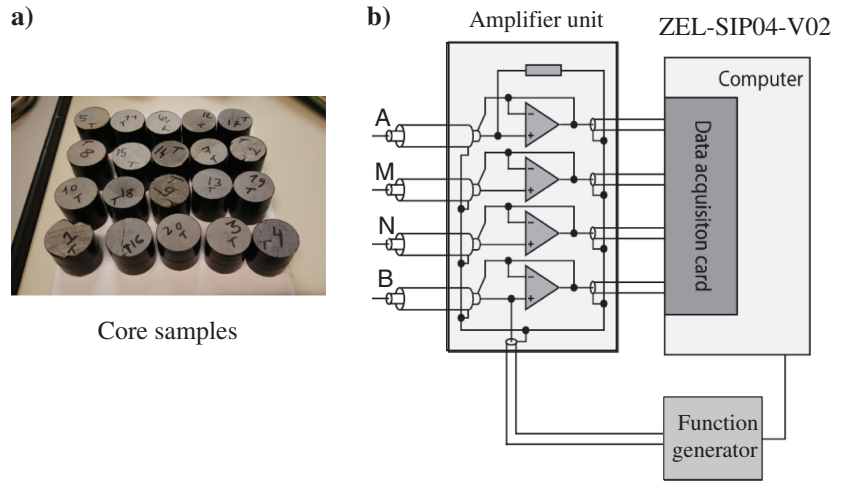

Figure 5. Core samples, impedance meter, and position of the electrodes on the sample holders. (a) Core samples with their insulating tape around them. The saturations are done under vacuum (less than 1 mbar). Samples #1, 2, 9, and 16 are fractured. (b) ZEL-SIP04-V02 impedance meter used for the laboratory experiments. This high-precision impedance meter was built by Zimmermann et al. (2008) in Julich (Germany).
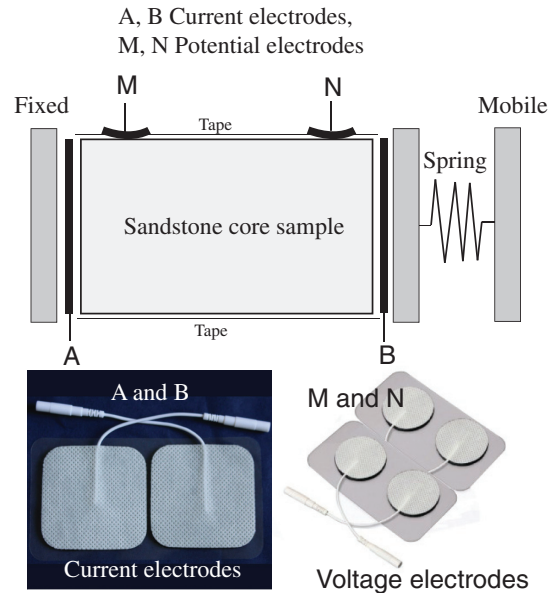

Figure 6. Sketch of the experimental setup for the consolidated core samples. The electrodes are self-adhesive superconductive carbon film, carbon/Ag/AgCl electrodes with biocompatible hydrogel commonly used in general and neonatal cardiology. Their impedance is 0.9 ohm over the frequency range investigated (0.1 Hz = 45 kHz). We did not use metallic pieces to minimize spurious polarization effects including through inductive and capacitive couplings. The electrodes are removed from the core samples after the measurements. The gel insures a uniform contact between the electrodes and the core sample that does not vary over time or experiments. We also avoided having the electrodes far from the sample itself to avoid the introduction of spurious resistances for the volume of brine sandwiched between the core and the electrodes.

for the electrical potential and considering the geometry of the bucket and the position of the electrodes (Figure 7). For materials with an electrical conductivity in the range $10^{-2} - 10$ S m^{-1}, the geometric constant was found to be $g = 16.6 \pm 0.1$ m^{-1}. The second procedure was to fill the sample holder with brines of measured conductivity (we used four brines in the range $0.01 - 1$ S m^{-1}) and measuring the resistance with the impedance meter. We found a geometric factor of 16.5 ± 0.5 m^{-1} independent on the conductivity. In the following, we use a geometric factor of 16.5 m^{-1} independent on the conductivity of the material in the bucket to interpret the impedance measurements.

All conductivity data reported are corrected of the effect of temperature using linear relationships $\sigma_w(T) = \sigma_w(T_0)(1 + \alpha_w(T - T_0))$ and $\sigma_S(T) = \sigma_S(T_0)(1 + \alpha_S(T - T_0))$, and therefore the temperature dependence of the conductivity is given by $\sigma * (T) = \sigma * (T_0)(1 + \alpha(T - T_0))$, and the conductivities are reported at 25°C using this equation, and where T_0 denotes the reference temperature $(T_0 = 25°C)$, T is the temperature of the solution, and $\alpha_w \approx \alpha_S \approx 0.02/°C = \alpha$ (e.g., Vinegar and Waxman, 1984). These equations mean that the temperature dependence of the in-phase and quadrature conductivities are due to the temperature dependences of the mobilities of the charge carriers, which in turn are controlled by the temperature dependence of the viscosity of the pore water.

Because the chargeability is a ratio of conductivity, this implies that chargeability is temperature independent, whereas the normalized chargeability has the same linear temperature dependence as described above.

For the other pore-water conductivities, the change of brine was done by diffusion by letting the samples in a tank in which the solution is at the desired salinity and to minimize the dissolution of the carbonates. Equilibrium was reached in a few weeks. The complex conductivity spectra were repeated over time, and the batch was considered to have reached equilibrium when the conductivity spectra were not changing over time.

Complex conductivity measurements

The complex conductivity measurement was conducted using the four-terminal method with a high-precision impedance analyzer (Figure 5; Zimmermann et al., 2008). The frequency range used on the ZEL-SIP04-V02 impedance meter is from 1 mHz to 45 kHz. For our measurements, we use imposed injection voltages of 5, 1, and 0.2 V. These three voltages are used to check the linearity of the response and to determine a standard deviation on the complex conductivity at each frequency.
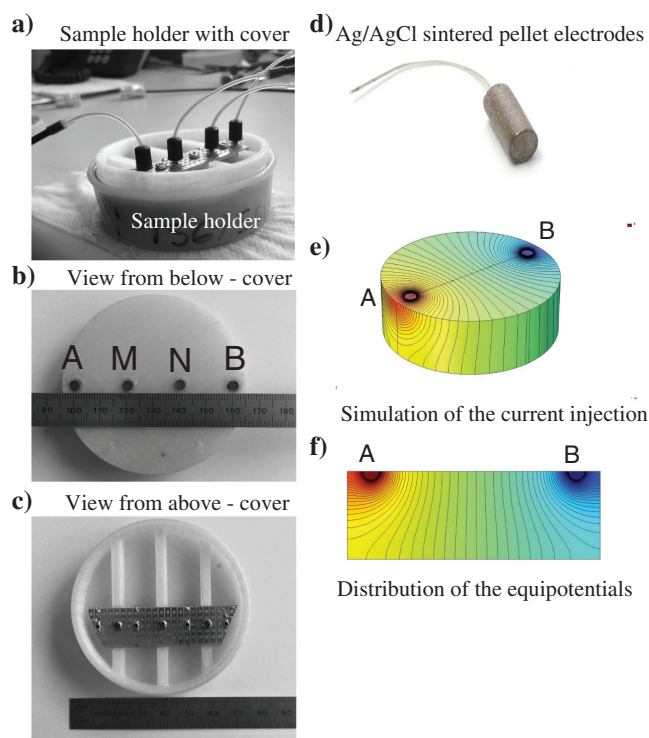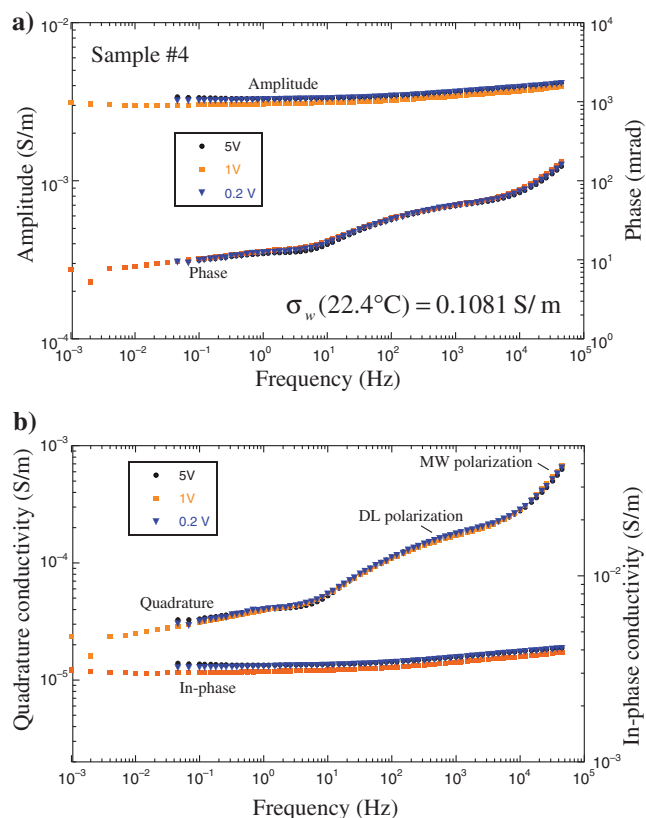

Figure 7. Sketch of the second experimental setup used for the unconsolidated core samples. (a) Picture of the sample holder with the 3D printed cover. (b and c). Picture of the cover with the encapsulated sintered electrodes. (d) We use Ag/AgCl sintered electrode for the A, B, M, and N electrodes. These sintered electrodes are made by compacting a very fine mixture of silver and silver chloride under high pressure. Sintered electrodes are known to provide less noisy signals by comparison with classical electrodes. Their impedance is approximately 90 ohm. (e and f) Simulation of the current injection and voltage distribution used to compute the geometric factor. The current probes a large portion of the samples.

Figure 8. Spectral-induced polarization data for sample #4 at a pore-water conductivity of 0.1081 S m^{-1} (NaCl, 22.4°C). (a) Amplitude of the conductivity and phase in the frequency range 1 mHz–45 kHz. The measurements are made at three voltage amplitudes (5, 1, and 0.2 V). (b) Complex conductivity spectra at the three same voltage amplitudes. MW stands for Maxwell-Wagner polarization (including the contribution of the high-frequency permittivity of the material), whereas the DL polarization corresponds to the polarization of the electrical DL.

An example of the complex conductivity spectrum is shown in Figure 8a for the amplitude and the phase. Then, the amplitude and the phase are used to determine the in-phase (real) conductivity and the quadrature (imaginary) conductivity spectra (Figure 8b).

CEC and SSA measurements

The CEC measurements were obtained with the NH_4 displacement method (Chapman, 1965). We used 4 g of material. The procedure follows the recipe provided by Chapman and Pratt (1978). The CEC data are provided in Table 2 and are expressed in meq/100 g (which is the traditional unit for this parameter). The range of values is 5–15 meq/100 g. These data can be converted in the international system of units using the following conversion: 1 meq/100 g = 963.20 $C\,kg^{-1}$. The SSA measurements were performed using the Micromeritics BET measurement system and interpreted with the BET method (see the details in Brunauer et al., 1938).

To show quickly the relevance of the CEC to quadrature conductivity spectra, in Figure 9, we show quadrature conductivity spectra

of four sandstones characterized by very distinct values of the CEC. This figure shows very clearly that the quadrature conductivity is going to be dependent on the CEC, a point that will be discussed further below. In Figure 10, we compare the CEC determined from the mineralogy (reported in Table 1) and the measured CEC. For each clay mineral (chlorite, kaolinite, illite, and smectite), we use a mean CEC value determined from Figure 1. We see a strong relationship between the two estimates indicating that most of the CEC is carried out by the clay minerals (as expected).

RESULTS

Shape of the spectra

We first show a few examples of the complex conductivity spectra of our samples. An example of complex conductivity spectra for sample #10 (sandstone) is shown in Figures 11 and 12 at two different salinities (one low and the other very high). As explained in the previous section, the measurements are done at three distinct

Table 2. Petrophysical data for the rock samples and sand smectite mixes.[6]

Sample ID	Porosity (%)	CEC (meq/100 g)	Formation factor F (−)	Surface conductivity (S/m)	σ'' (S/m)	Ssp (m²/g)	Grain density (g/cm³)
20161501	11.13	13.1	20.8 ± 0.4	0.088 ± 0.006	1.50E-03	15.750	2.68
20161502	11.96	12.5	19.0 ± 0.4	0.113 ± 0.001	1.54E-03	15.750	2.71
20161503	6.58	11.0	49.5 ± 0.7	0.056 ± 0.001	6.98E-04	12.190	2.72
20161504	1.57	4.00	1757 ± 63	0.0031 ± 0.0001	1.78E-04	6.1700	2.72
20161505	5.61	11.6	51.7 ± 1.4	0.055 ± 0.004	8.09E-04	16.790	2.72
20161506	6.28	9.90	42.9 ± 1.2	0.066 ± 0.005	1.28E-03	15.080	2.75
20161507	3.09	7.30	292 ± 8	0.021 ± 0.002	3.04E-04	9.5000	2.71
20161508	2.43	4.30	1949 ± 258	0.0075 ± 0.0006	3.84E-04	7.1800	2.70
20161509	12.25	15.5	16.1 ± 0.2	0.105 ± 0.006	2.42E-03	13.070	2.71
20161510	4.27	7.80	243 ± 10	0.0277 ± 0.0015	4.67E-04	10.110	2.71
20161511	2.38	9.70	197 ± 1	0.0249 ± 0.0002	4.57E-04	12.270	2.70
20161512	0.820	7.20	485 ± 55	0.0162 ± 0.0020	1.57E-04	9.7500	2.69
20161513	3.78	6.50	596 ± 3	0.0146 ± 0.0001	2.85E-04	7.9200	2.71
20161514	3.10	8.60	287 ± 9	0.0192 ± 0.0007	3.21E-04	9.3300	2.71
20161515	6.11	15.3	51 ± 2	0.0716 ± 0.0042	1.19E-03	14.750	2.71
20161516	5.17	6.50	169 ± 4	0.0229 ± 0.0010	5.10E-04	7.0200	2.69
20161517	2.56	5.20	1461 ± 143	0.0030 ± 0.0005	5.90E-05	6.8700	2.69
20161518	4.52	9.00	392 ± 12	0.0217 ± 0.0009	3.83E-04	9.0300	2.71
20161519	4.39	12.8	98 ± 4	0.0431 ± 0.0029	1.74E-03	13.230	2.71
20161520	3.76	10.6	92 ± 1	0.0563 ± 0.0019	6.31E-04	15.130	2.70
S100	90	75	1.7 ± 0.1	0.166 ± 0.009	4.36E-03[(3)]	31.8	2.65
Sd95	58	3.8[(1)]	4.8 ± 0.3	0.056 ± 0.007	4.36E-03[(3)]	1.6	2.65
Sd90	47	7.5[(1)]	4.0 ± 0.2	0.091 ± 0.003	6.54E-03[(3)]	3.2	2.65
Sd100	52	0.0027[(2)]	4.3 ± 0.1	0.0041 ± 0.0009	~1 E − 05	—	2.65

[6]The formation factor and the surface conductivity are determined at four salinities. Sandstones 20161501 (abbreviated as sample #1 in the main text), 20161502 (#2), and 20161508 (#9) are damaged with visible cracks. Samples (#3, #5, #9, #10, #11, #16, and #19) show some small cracks. The other samples are intact. For the sandstones, surface conductivity is determined at 100 Hz (close to the relaxation peak). The smectite corresponds to the SWy-2-smectite from the clay mineralogical society. CEC and Ssp denote the CEC and SSA, respectively. (1) The CEC and SSA are computed form the CEC or SSA of pure smectite and the weight fraction of smectite in the core sample. (2) For silica grains, the equivalent CEC is given by CEC = $6Q_S/(\rho_s d)$ with a surface charge density of $Q_S = 0.64\ C\,m^{-2}$, d is the diameter of the sand grains, and $\rho_s = 2650\ kg\,m^{-3}$ denotes the mass density of the silica grains. We use a grain diameter of 550 µm and the conversion factor 1 $cmol\,kg^{-1}$ = 1 meq/(100 g) = 963.2 $C\,kg^{-1}$. (3) Determined at a pore-water conductivity of 0.1 $S\,m^{-1}$ (25°C, NaCl).

applied voltages 0.2, 1, and 5 V, which allows testing of the linearity of the system (the amplitude response should be proportional to the amplitude of the driving force). From such data, we can decide that the rock samples behave linearly. Less than 0.1 Hz, the phase is generally too small to be accurately measured. Our sandstones are observed to display a broad relaxation peak in the frequency range of 10–1000 Hz. At higher frequencies (greater than 10 kHz), the increase of the magnitude of the quadrature conductivity is due
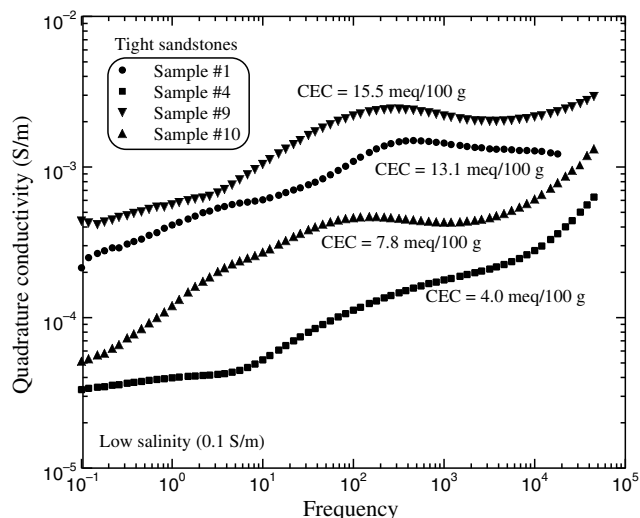
Figure 9. Example of four quadrature conductivity spectra characterized by four distinct values of the CEC. These spectra are obtained at low salinity (approximately 0.1 S m^{-1}). We can observe that the magnitude of the quadrature conductivity is correlated with the CEC. Note: 1 meq/(100 g) = 963.2 C kg^{-1}. The shape of the spectra is expected to reflect the distribution of the polarization length scales.
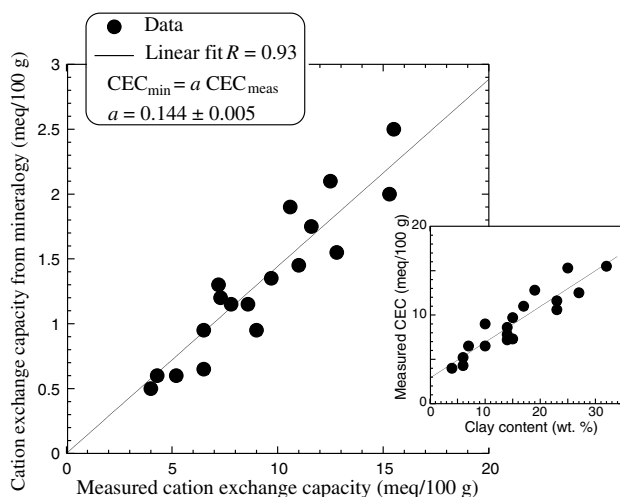
Figure 10. CEC determined from the weight fraction of the clay minerals (kaolinite, chlorite, illite, and smectite) with respect to the total mass of solid and measured CEC. We use the following CEC values for the individual clay fractions: CEC(K, C) = 5 meq/100 g, CEC(I) = 20 meq/100 g, and CEC(S) = 75 meq/100 g. Note that two samples have been omitted. Insert: correlation between the measured CEC and the clay content (wt%, R = 0.93).
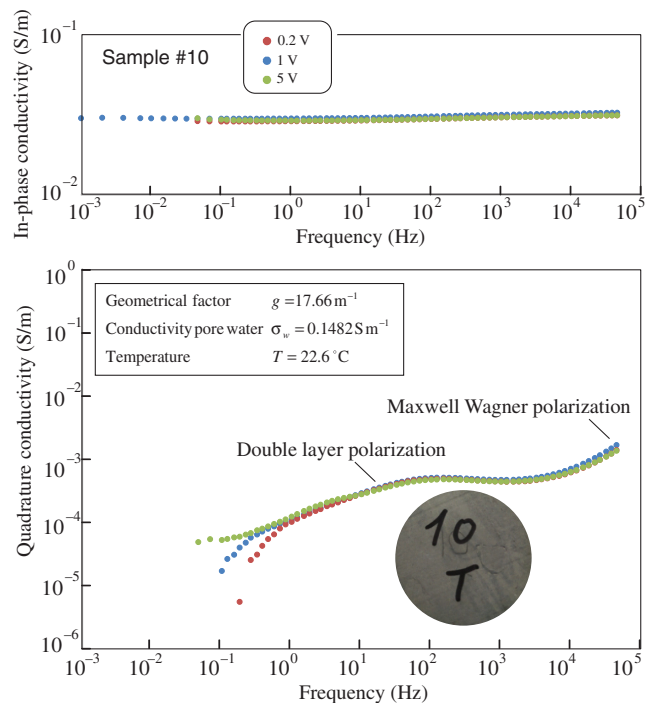
Figure 11. Sample #10 at the lowest salinity (sandstone). The quadrature conductivity spectra are showing the Maxwell Wagner polarization and the DL polarization.
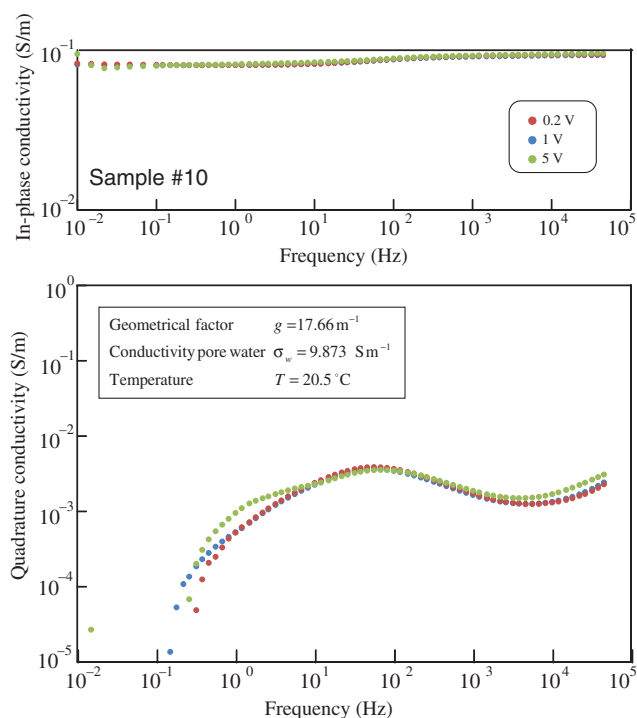

Figure 12. Complex conductivity spectra of sample #10 (sandstone) at the highest salinity (pore-water conductivity 10 S m^{-1}) at three different applied voltages.

to the Maxwell Wagner effect and true dielectric effects. As expected, the spectrum of the in-phase conductivity is rather flat; i.e., the percentage frequency effect (PFE) is rather small, as discussed below.

Figures 13, 14, and 15 correspond to the response for the sand-clay mixtures at different salinities. The smectite polarizes at very high frequency (10 kHz) likely due to the very small size of the particles. We do not see a strong response of the quadrature conductivity with the salinity for these mixtures. This is likely due to the fact that smectite has essentially a surface charge density that does not change with the salinity because it is due to isomorphic substitutions in the crystalline framework. Oppositeli, illite has a surface charge that is controlled by the amphoteric sites at the edges of the crystals, and therefore the surface charge density of illite is salinity-dependent. We will see that this is the case for the sandstones investigated in the present work and that are illite-rich (Table 1).

In Figure 16, we look at the dependence with the salinity of the quadrature conductivity of the sandstones. We observe that the smectite-rich samples and the illite-rich samples exhibit a distinct behavior with the salinity. Niu et al. (2016b) explain the dependence of the magnitude of the quadrature conductivity with the salinity in terms of electrochemical effects involving the surface speciation of the clay-mineral surfaces. Comparing this model with the data set is out of the scope of the present investigation, and it would require measurements on a broader salinity range.

Normalized chargeability versus quadrature conductivity

The FE is defined from the variation with the frequency of the magnitude of the electrical conductivity (approximated here by the in-phase conductivity; see Vinegar and Waxman, 1984)

$$\mathrm{FE} \approx \frac{\sigma'(A\omega) - \sigma'(\omega)}{\sigma'(A\omega)} \geq 0. \tag{23}$$

In other words, the FE characterizes the increase in the in-phase conductivity between two angular frequencies ω and $A\omega$. This FE can be in turn related to the phase angle φ (phase lag in rad) measured at the geometric frequency $A^{1/2}\omega$ (see Shuey and Johnson, 1973; Van Voorhis et al., 1973). This relationship can be obtained using two distinct complex resistivity models (see Appendix C for details)

$$\mathrm{FE} \approx -\frac{2}{\pi}\varphi \ln A, \quad \text{for } \varphi \ll 1. \tag{24}$$

We chose to check the consistency of the complex conductivity spectra over one decade (i.e., $A = 10$). In this case, the PFE is given by PFE $= 100 \, \mathrm{FE} \approx 0.1467\varphi$ (Vinegar and Waxman, 1984) with the phase directly expressed in mrad. In Figure 17, we use all of the sample data (sandstones) to study if this relationship is obeyed for the in-phase conductivity measured between 1 and 10 Hz, 10 and 100 Hz,
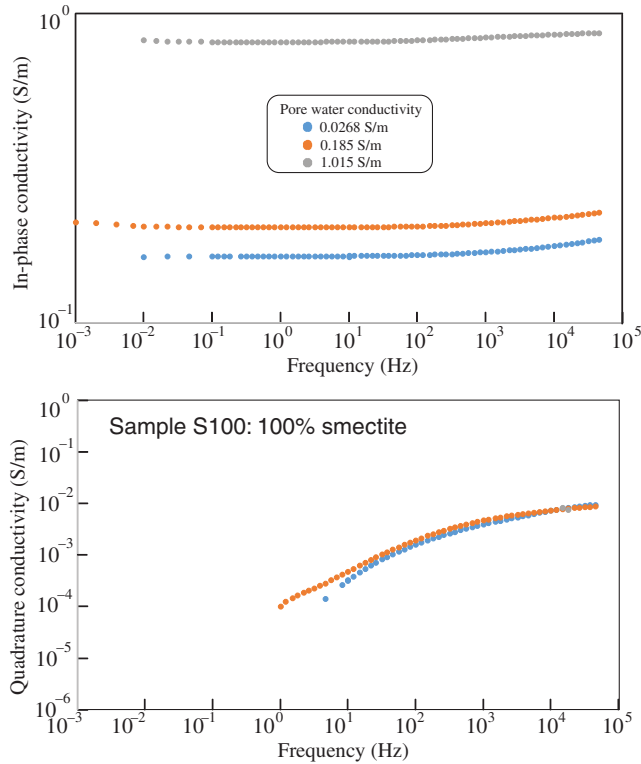

Figure 13. Sample S100 (100% smectite) at three salinities. Although the in-phase conductivity depends a lot on the pore-water conductivity, the quadrature conductivity seems independent on the pore-water conductivity. Because of the small size of the clay particles, the polarization of smectite takes place at high frequencies (greater than 1 kHz).
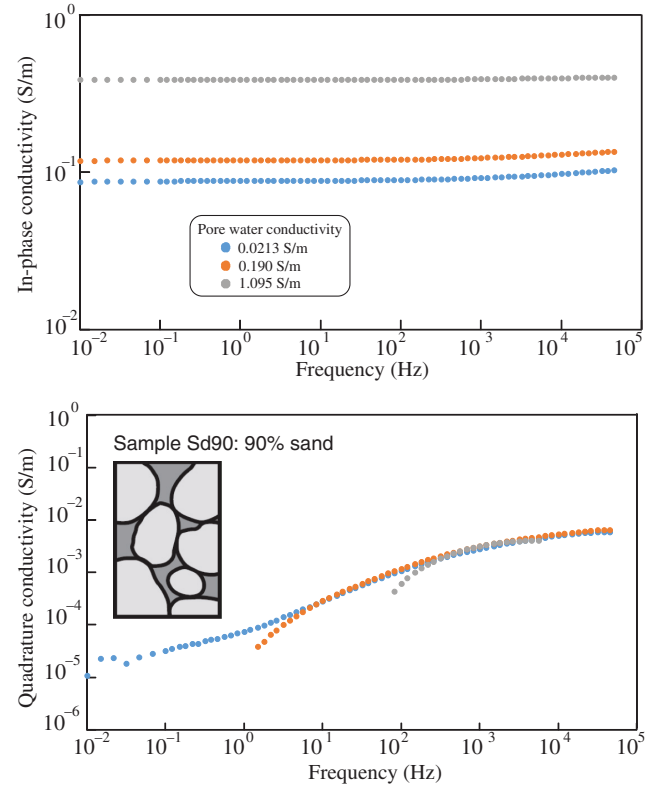

Figure 14. Sample Sd90 (90% sand) at the three salinities. As for the pure smectite, the in-phase conductivity depends on the pore-water conductivity, whereas the quadrature conductivity seems to be quite independent of the pore-water conductivity. The high-frequency behavior is likely dominated by the smectite, whereas the low-frequency behavior is dominated by the silica grains.
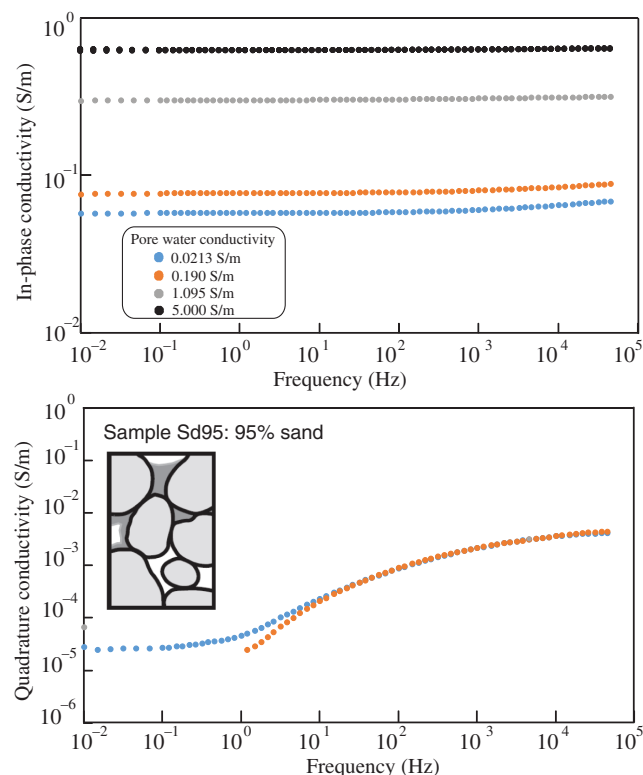
Figure 15. Sample Sd95 (95% sand) at the three salinities. Note that the quadrature conductivity seems to be independent of the pore-water conductivity. The high-frequency behavior is likely dominated by the smectite, whereas the low-frequency behavior is dominated by the silica grains. The quadrature conductivity data at high salinities are not reported because of large uncertainties in their determination, which is in turn associated with the small value of the phase.
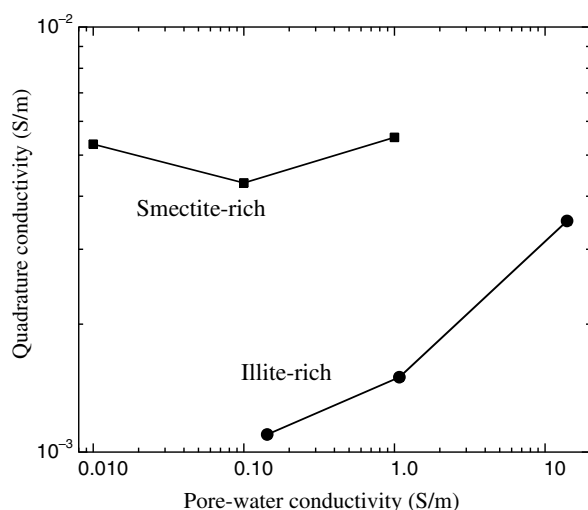

Figure 16. Salinity dependence of the quadrature conductivity. Data taken at 100 Hz for the illite-rich sandstone and 10 kHz for the smectite and the two sand-smectite mixes. For the sandstones, the reported values are the average for six samples characterized by the same normalized CEC ($CEC/F\phi = 5 \pm 2$ meq/100 g).
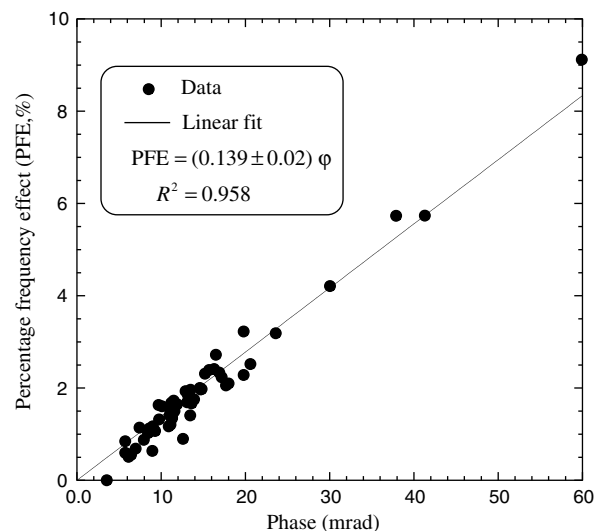
Figure 17. Relationship between the PFE and the phase ϕ (positive for the impedance) for the low-salinity data. The theoretical prediction PFE $= 100$ FE $\approx 0.1467\varphi$ (see Vinegar and Waxman, 1984) is also shown for comparison. The in-phase conductivity is measured between 1 and 10 Hz, 10 and 100 Hz, and 100 Hz and 1 kHz, and the phase is determined at the geometric mean of the two frequencies (i.e., 3.2, 32, and 320 Hz, respectively). We used only the data at the lowest salinity for each sample. The points outside the trends are considered to be problematic. Note that the phase can reach 60 mrad in amplitude, whereas the PFE remains less than 10%.
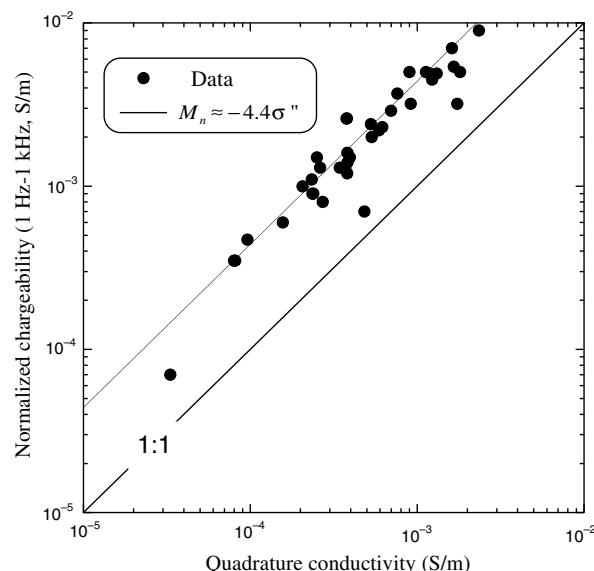

Figure 18. Relationship between the normalized chargeability and the quadrature conductivity for the lowest salinity data set and for the salinity corresponding to 1 S m^{-1}. The normalized chargeability is defined as the difference in the in-phase conductivity between the two frequencies (in the present case, 1 Hz to 1 kHz). In other words, the normalized chargeability is computed in the frequency range 1 Hz to 1 kHz (the quadrature conductivity is determined at the geometric mean, i.e., 32 Hz). The theoretical prediction $M_n \approx -4.4\sigma''$ is also shown for comparison. The points outside the trend are considered to be problematic.

and 100 Hz and 1 kHz and the phase measured at the geometric mean (3.2, 32, and 320 Hz, respectively). We obtain PFE = 0.139φ, pretty close to the predicted trend.

Equation 23 can be used to determine the relationship between the quadrature conductivity and the normalized chargeability. We assume that the conductivity itself is not a strong function of the frequency, which is the case for porous rocks (see Vinegar and Waxman [1984] and the magnitude of PFE in Figure 17). Then, we consider that the quadrature conductivity is determined close to the peak frequency used as the geometric mean frequency between a low frequency for which the conductivity is close to σ_0 and a high frequency for which the conductivity is close to σ_∞. In this case, equation 23 can be written as an equation connecting the normalized chargeability and the quadrature conductivity

$$M_n \approx -\left(\frac{2}{\pi}\ln A\right)\sigma'', \qquad (25)$$

where A is the number of decades separating the high and low frequencies. Equation 24 provides a direct way to estimate the value of α in equation 17. Comparing the two equations, we have indeed

$$\alpha \approx -\left(\frac{2}{\pi}\ln A\right). \qquad (26)$$

We compare in Figure 18, the normalized chargeability between 1 Hz and 1 kHz and the quadrature conductivity determined at the geometric mean frequency of 32 Hz. This normalized chargeability is defined as the difference in the in-phase conductivity between 1 kHz and 1 Hz. The data shown in Figure 18 exhibit a very high linear trend with a slope $\alpha = 4.4$. consistent with the theoretical prediction corresponding to equation 25.

In Figure 19, we compare the normalized chargeability now determined over the frequency range 0.1 Hz–10 kHz (so over five decades; i.e., $A = 10^5$) with the quadrature conductivity determined at the geometric mean frequency of 32 Hz. The data shown in Figure 19 exhibit a linear trend with a slope of 5.2 slightly below the theoretical prediction $\alpha = 7.3$. From the linear relationship between the quadrature conductivity and the normalized chargeability, we can say that all the observations made between the quadrature conductivity, the CEC, the SSA, or the clay content are also valid for the normalized chargeability.

Application of the linear conductivity model

We plot now the conductivity data (in-phase conductivity determined at 100 Hz) versus the pore-water conductivities for the three or four NaCl solutions (see Figures 20, 21, and 22). The data are fitted with equation 5 to determine the (intrinsic) formation factor F and the surface conductivity σ_s. The results are reported in Table 2. In Figure 23, we plot the (intrinsic) formation factors reported in Table 2 for each sample
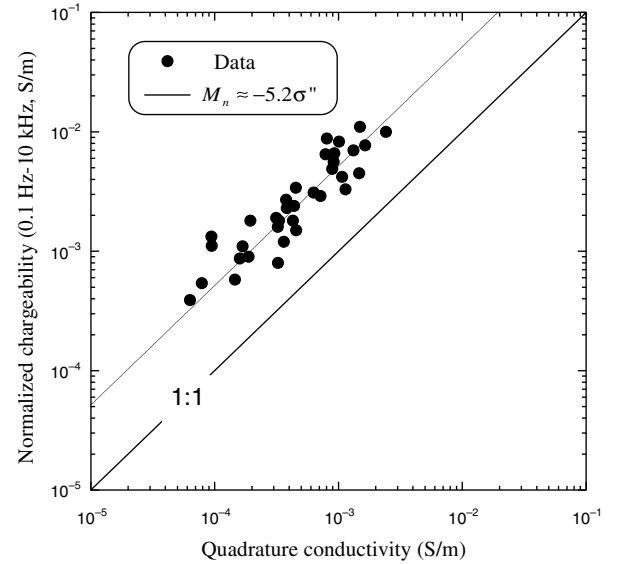

Figure 19. Relationship between the normalized chargeability M_n and the quadrature conductivity (at the geometric frequency of 32 Hz) for the low and intermediate salinity data sets (0.1 and 1 S m^{-1}) and the frequency range 0.1 Hz to 10 kHz. The normalized chargeability is defined as the difference in the in-phase frequencies between the two frequencies (in the present case, 0.1 Hz to 10 kHz). The theoretical prediction for the trend is $M_n \approx -7.3\sigma''$, so slightly above the trend shown by the data. The points outside the trend are considered to be problematic.
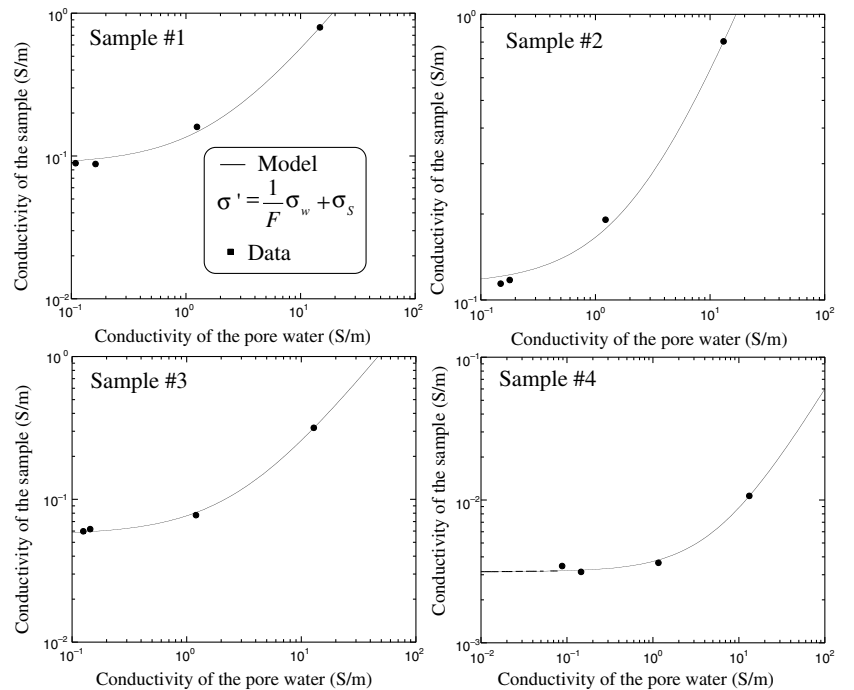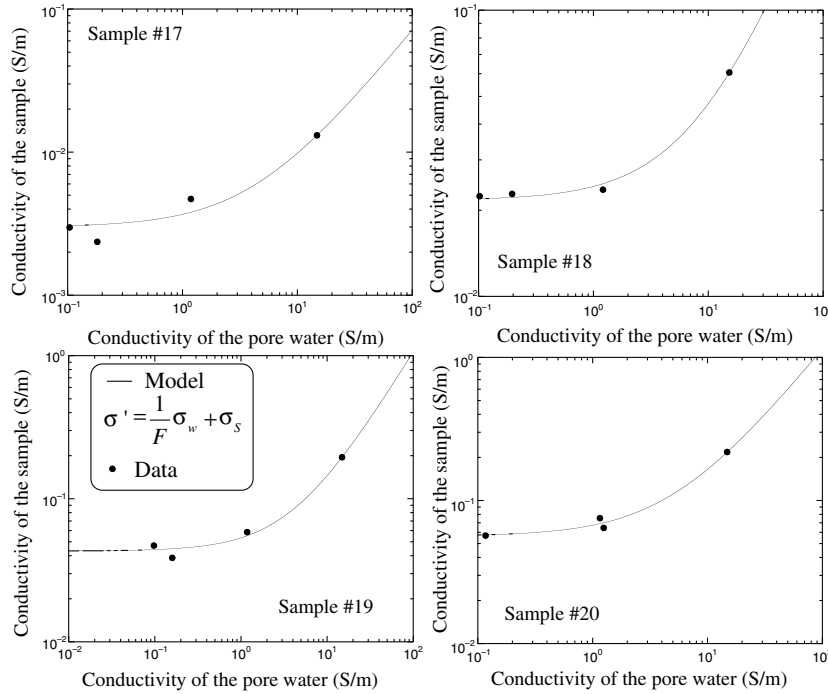

Figure 20. Example of data sets between the in-phase conductivity of four sandstones (at 100 Hz) and the conductivity of the pore water at four salinities (NaCl solutions). The data are fitted with equation 5 (plain lines) to determine the (intrinsic) formation factor F and the surface conductivity σ_s, which are reported in Table 2.

versus their corresponding porosities. We fit the data set with the modified Archie's (1942) law $F = (\phi - \phi_p)^{-m}$ using a percolation threshold for the porosity ϕ_p. We obtain an average cementation exponent m of 1.5 ± 0.1 with a percolation porosity ϕ_p of 0.01. We note that the value of the cementation exponent is surprisingly small. The insert in Figure 23 shows that the samples exhibiting cracks actually have a cementation exponent between 1.3 and 1.5, whereas the samples that look undamaged are characterized by a cementation exponent between 1.7 and 2.1.

Surface conductivity and CEC

In Figure 24, we report the surface conductivity (at 100 Hz) versus the normalized CEC (i.e., the CEC divided by the tortuosity of the bulk pore space, i.e., given by the product between the formation factor and the porosity). This trend is indeed predicted by the dynamic Stern layer model. We observe an excellent relationship between the surface conductivity and the normalized CEC. The relationship between the surface conductivity and the CEC is $\sigma_S = \rho_g B (\text{CEC}/F\phi)$; therefore, factor "$a$" given in Figure 24 is equal to $\rho_g B$ (the grains density is 2700 kg m^{-3}; see Table 2). This yields an apparent mobility $B = 1.63 \times 10^{-8}$ m^2 s^{-1} V^{-1} at 25°C.

Quadrature conductivity and normalized chargeability versus CEC

In Figure 25, we report the quadrature conductivity (at 100 Hz) versus the normalized CEC (i.e., the CEC divided by the tortuosity of the bulk pore space, i.e., given by the product between the formation factor and the porosity). The trends are estimated at two distinct salinities. We observe a fair linear relationship between the two parameters as predicted by our model, but with a residual quadrature conductivity of approximately -6×10^{-5} S m^{-1}. The sandstones are characterized by the presence of some pyrite (see Table 1). Consequently, it may be possible that this residual quadrature conductivity (also observed by Vinegar and Waxman, 1984) could be related to this mineral. Indeed, pyrite is a semiconductor characterized by strong polarization, as discussed, for instance, by Pelton et al. (1978) and Mao et al. (2016). In Figure 26, we show that the normalized chargeability $M_n(\omega, A\omega) \approx \sigma'(A\omega) - \sigma'(\omega)$ is also proportional to the normalized CEC in agreement with the dynamic Stern layer model.

Quadrature versus surface conductivities

In Figure 27, we plot the quadrature conductivity versus the surface conductivity for the 20 core samples. We can see that the data are consistent with other data sets obtained in the literature for sedimentary and volcanic rocks. The samples are, however, characterized by much higher surface and quadrature conductivities. The trend is consistent with a value of — $\sigma''/\sigma_S = 0.018 \pm 0.002$ for the ratio between the quadrature and surface conductivities; therefore, because $-\sigma''/\sigma_S = R/\alpha$ (and using $\alpha = 5$; see Figure 19), we obtain $R = 0.09$ in equations 18 and 19.

In Figures 28 and 29, we compare our data set with respect to a broader data set looking at the direct correlation between the surface conductivity and the CEC and the quadrature conductivity and the CEC, respectively. Looking at these trends, it is really clear that the effect of

Figure 21. Example of data sets between the in-phase conductivity of four sandstone samples (at 100 Hz) and the conductivity of the pore water at three or four salinities (NaCl solutions). The data are fitted with equation 5 (plain lines) to determine the (intrinsic) formation factor F and the surface conductivity σ_s (at 100 Hz), which are reported in Table 2.
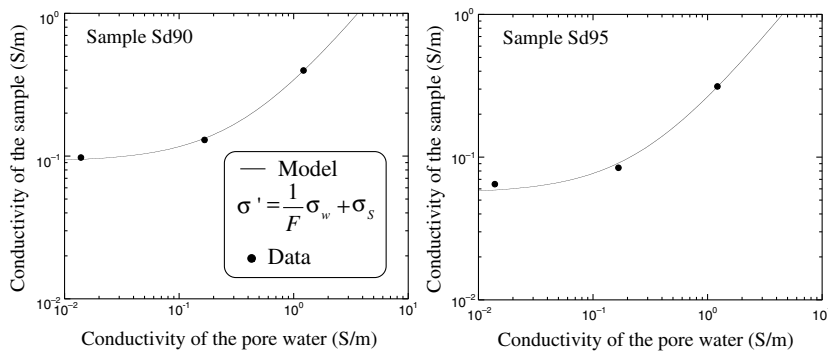

Figure 22. Example of data sets between the conductivity the sand clay mixes (in-phase conductivity at 100 Hz) and the conductivity of the pore water at three salinities (NaCl solutions). The data are fitted with the linear conductivity equation (plain lines) (equation 5) to determine the (intrinsic) formation factor F and the surface conductivity σ_s.
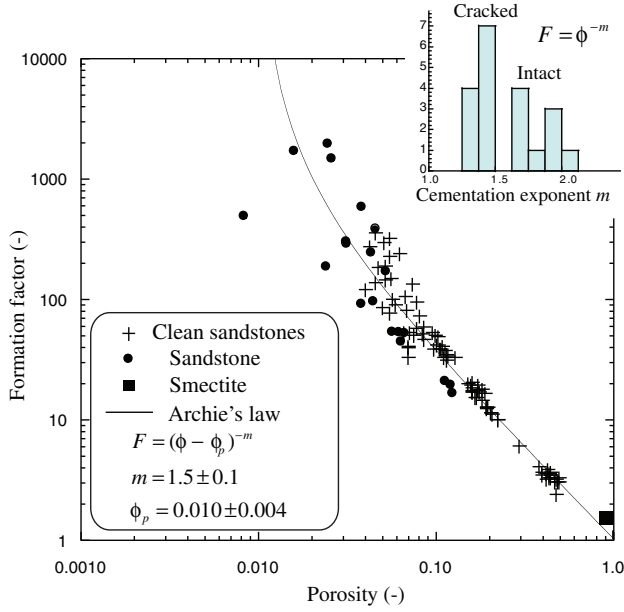
Figure 23. Relationship between the formation factor and the porosity and fit using the Archie's (1942) law and the modified Archie's law with a percolation threshold (Sen et al., 1981). We used here all the samples from this study for the 20 sandstone core samples. We also added the data for the Fontainebleau sandstones and clean sands reported by Revil et al. (2014b) for comparison. Inset: cementation exponent m obtained using Archie's law $F = \phi^{-m}$ for the 20 sandstones. The value of the cementation exponent of the nondamaged samples is between 1.6 and 2.1, whereas the samples with cracks have a cementation exponent comprised between 1.3 and 1.5.
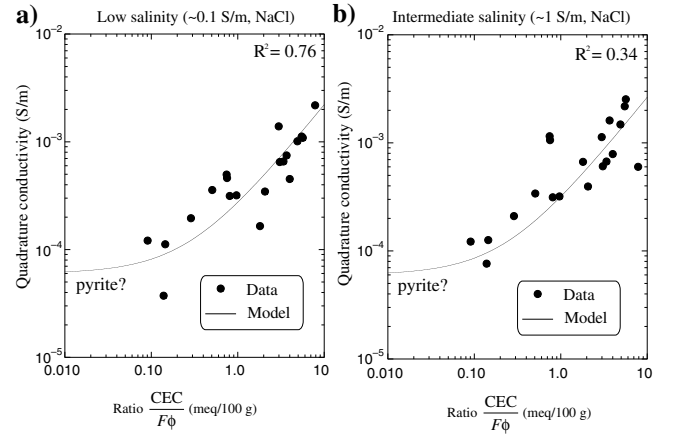

Figure 25. Relationship between the absolute value of the effective quadrature conductivity (at a pore-water conductivity of approximately 0.1 and 1 $S\,m^{-1}$ and taken at 100 Hz) and normalized CEC (i.e., the CEC divided by the tortuosity of the bulk pore space). Indeed, according to our model, the quadrature conductivity should scale as the CEC divided by the tortuosity of the bulk pore space determined as the product of the (intrinsic) formation factor by the (connected) porosity (see equations 7 and 17). The slopes are $(2.6 \pm 0.4) \times 10^{-4}$ and $(2.2 \pm 0.2) \times 10^{-4}$ in the units used in the graph $(S\,m^{-1}(meq/100\,g)^{-1})$. Note: 1 meq/(100 g) = 963.2 $C\,kg^{-1}$.

Figure 24. Relationship between surface conductivity and normalized CEC. According to our model, the surface conductivity should scale as the CEC divided by the tortuosity of the bulk pore space determined as the product of the (intrinsic) formation factor by the (connected) porosity (see equation 6). Slope "a" is $(157 \pm 7) \times 10^{-4}$ in the units given in the graph $(S\,m^{-1}(meq/100\,g)^{-1})$. Note: 1 meq/(100 g) = 963.2 $C\,kg^{-1}$.
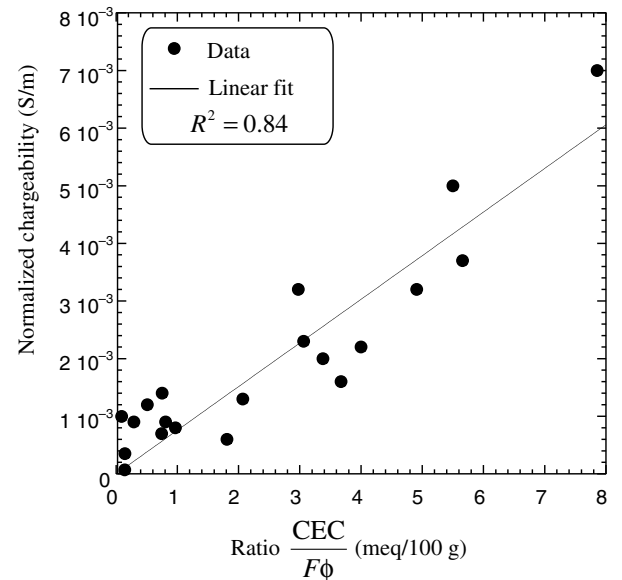

Figure 26. Relationship between the normalized chargeability (at a pore-water conductivity of approximately 0.1 $S\,m^{-1}$) and normalized CEC (i.e., CEC divided by the tortuosity of the bulk pore space). According to the dynamic Stern layer model, the normalized chargeability should scale as the CEC divided by the tortuosity of the bulk pore space determined as the product of the (intrinsic) formation factor by the (connected) porosity. The slope is $(75 \pm 5) \times 10^{-5}$ in the units used in the graph $(S\,m^{-1}(meq/100\,g)^{-1})$. Note: 1 meq/(100 g) = 963.2 $C\,kg^{-1}$.

the bulk tortuosity on the quadrature and surface conductivity cannot be overlooked. That said, the effect on the ratio of the two quantities is null or, in other words, the surface and quadrature conductivities have the same dependence with the bulk tortuosity.

Mobility of the counterions and partition coefficient

The trends shown in Figures 24 and 25 can be used to determine the mobilities of the counterions and the partition coefficient between the Stern and diffuse layers. Starting with the apparent mobility for surface conductivity $B = \beta_{(+)}(1-f) + \beta_{(+)}^S f$ and equation 19, and after a few algebraic manipulations, we obtain

$$f = 1 - \frac{B(1-R)}{\beta_{(+)}}. \qquad (27)$$

Because we already determined the values of the three parameters entering this equation 26 ($B = 1.63 \times 10^{-8}$ m^2 V^{-1} s^{-1} see the "Surface conductivity and CEC" section, $R = 0.094$ from the trend shown between surface and quadrature conductivity in Revil et al. (2017a), and finally $\beta_{(+)}(Na^+, 25°C) = 5.2 \times 10^{-8}$ m^2 s^{-1} V^{-1}, the mobility of sodium in water), we obtain $f = 0.74$. In other words, 74% of the counterions are located or partitioned in the Stern layer. We can also determine the value of the mobility of the cations in the Stern layer. Starting with the same equations, we obtain

$$\beta_{(+)}^S = \beta_{(+)} \frac{R(1-f)}{f(1-R)}. \qquad (28)$$

Taking $\beta_{(+)}(Na^+, 25°C) = 5.2 \times 10^{-8}$ m^2 s^{-1} V^{-1}, $R = 0.094$, and $f = 0.74$, we obtain $\beta_{(+)}^S = 1.9 \times 10^{-9}$ m^2 s^{-1} V^{-1}, and therefore a ratio $\beta_{(+)}/\beta_{(+)}^S \approx 27$. The mobility of the counterions in the Stern layer is 27 times smaller than in the diffuse layer in agreement with Revil et al. (2017a, 2017b) for volcanic rocks.

DISCUSSION

We discuss now the value of the concept of normalized chargeability for porous media with no metallic particles. We first plot the normalized chargeability versus the surface conductivity (Figure 30). For our data, the two quantities are proportional, which means that we can use time-domain induced polarization data to compute the surface conductivity required to properly interpret resistivity tomograms or well-log data in field conditions. Interestingly, as shown in Appendix A, the normalized chargeability for the rock denotes actually a normalized chargeability for the surface conductivity itself (at least in the linear model used in this paper). So, this means that the frequency variation for the surface conductivity is proportional to the magnitude of the surface conductivity itself.

In this work, we have shown that the surface conductivity, the quadrature conductivity, and the normalized chargeability of tight
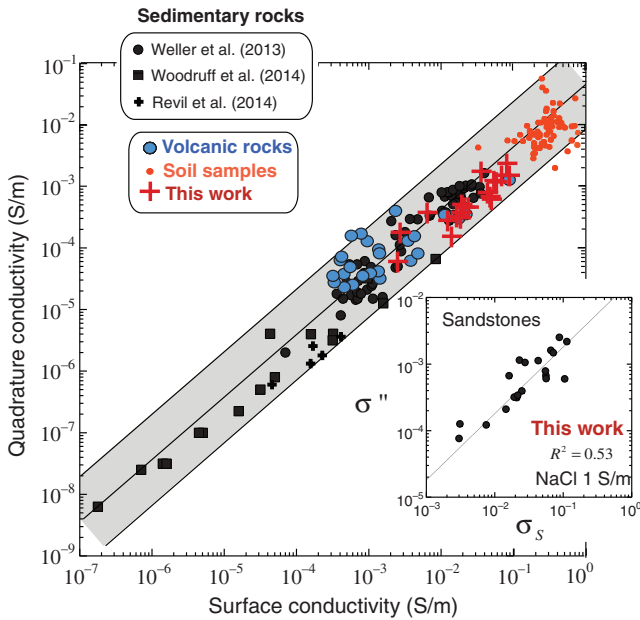

Figure 27. Relationship between quadrature conductivity and surface conductivity over seven orders of magnitude. The soil samples are from the Netherlands (Revil et al., 2017c). The data for the volcanic rocks are from Revil et al. (2017a, 2017b). All data show that the ratio of the quadrature to surface conductivity is independent of the bulk tortuosity of the connected pore space. For the tight sandstones, the quadrature conductivity data are taken at a pore-water conductivity of approximately 1 S m^{-1} and at 1 kHz. Other data are from Weller et al. (2013) (sands and sandstones), Woodruff et al. (2014) (oil and gas shales), and Revil et al. (2014b) (Fontainebleau sandstones). For the 20 sandstones investigated in the present study (see inset), we have — $\sigma''/\sigma_S = 0.018 \pm 0.002$, i.e., $R = 0.094$. Note that this trend is independent of the value of the formation factor and tortuosity of the conduction current.
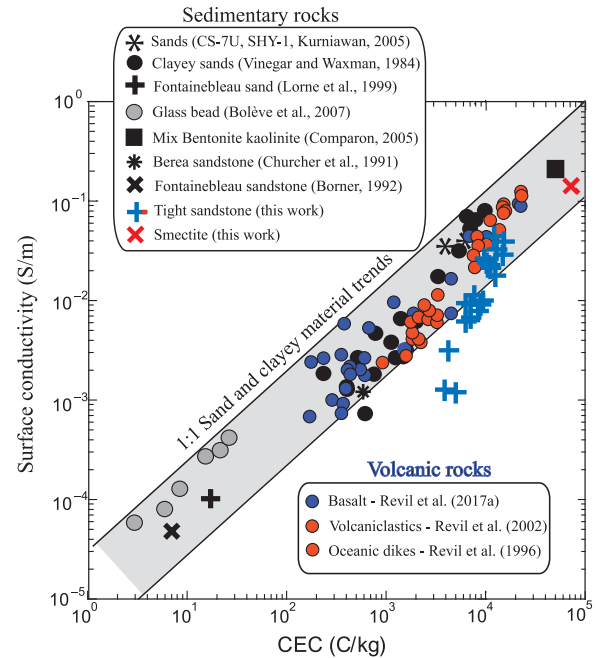

Figure 28. Relationship between surface conductivity and CEC. We clearly see the effect of tortuosity from our data set on the trend between the surface conductivity and the CEC because the samples with the lowest surface conductivity correspond to the samples with the highest tortuosity in our data set. Note: 1 meq /(100 g) = 963.2 C kg^{-1}. The data from the literature are from Bolève et al. (2007) (glass beads, NaCl), Vinegar and Waxman (1984) (shaly sands, NaCl), Churcher et al. (1991) (CEC for the Berea sandstone), Lorne et al. (1999) (Fontainebleau sand KCl), Kurniawan (2005) (clean sand, sample CS-7U), Börner (1992) (sample F3 Fontainebleau sandstone), and Comparon (2005) (mixtures of MX80 bentonite and kaolinite).
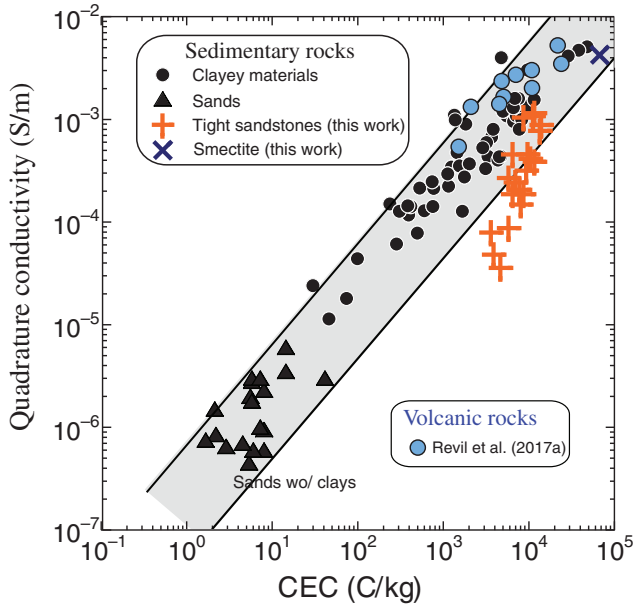
Figure 29. Relationship between quadrature conductivity (for the tight sandstones reported at 1 S m⁻¹ and 1 kHz) and CEC. We clearly see the effect of tortuosity from our data set on the trend between the quadrature conductivity and the CEC. For the sedimentary rocks, the quadrature conductivity is obtained at the relaxation peak. These data show that for clayey media and "dirty" sands, the quadrature conductivity close to the relaxation peak is proportional to the CEC (the data are those discussed in Revil et al., 2015). Note: 1 meq/(100 g) = 963.2 $C\,kg^{-1}$.
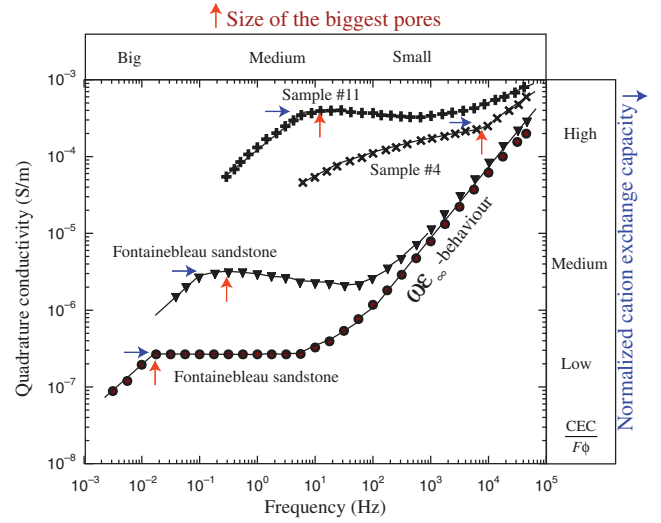
Figure 31. Sketch showing for different sandstones how the plateau (blue arrows) is grossly associated with the normalized CEC (CEC divided by the product of the intrinsic formation factor by the porosity) and the characteristic frequency (red arrows) is related to the pore size. The Fontainebleau data are from Revil et al. (2015). The quantity ε_∞ denotes the high-frequency permittivity, which is actually the low-frequency part of the Maxwell Wagner polarization. This plot also shows that depending on the value of the CEC of the core sample, the effective quadrature conductivity can be affected by the high-frequency dielectric effect.

sandstones scales with the CEC of the material divided by the bulk tortuosity (the product of the formation factor by the porosity; see Figure 29). Because the CEC and the SSA are proportional to each other, this means that in our case the surface conductivity, the quadrature conductivity, and the normalized chargeability of tight sandstones scales with the SSA divided by the product of the formation factor and the porosity. When the dominant clay type is constant, this also means that the surface conductivity, the quadrature conductivity, and the normalized chargeability of tight sandstones scale with the clay content. In Figure 31, we also show that there is a critical frequency that seems to scale with the pore size. In the next paper of this series, we plan to investigate in more detail the relationship between the pore size (and the pore-size distribution) and the critical relaxation time (and the distribution of relaxation times). Our goal is also to show what method is the most appropriate to decompose the spectra in terms of their distribution of the relaxation times given by equation 1 (see the discussion in Niu et al., 2016a). This will be the purpose of a future paper.
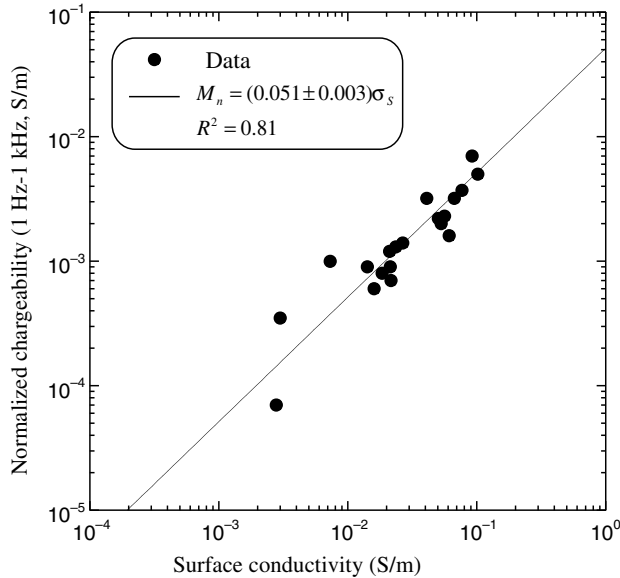

Figure 30. Relationship between the normalized chargeability and the surface conductivity. The normalized chargeability is here defined as the difference in the in-phase conductivity between two frequencies (in the present case 1 Hz to 1 kHz).

CONCLUSION

We have studied a collection of 20 tight sandstones plus four sand-clay mixtures using a sand and a smectite. The samples are characterized by very high cation exchange capacities, surface conductivities, and quadrature conductivities, which all scale with the CEC, the SSA, or the clay content (in weight and at a constant mineralogy). The quadrature conductivity, normalized chargeability, and surface conductivity are found to be sensitive to the inverse of the product of the formation factor with the porosity. Such scaling agrees with a low-frequency polarization model based on the dynamic Stern layer model, but it cannot be found in an alternative

model such as the membrane polarization model. We have found that the cementation exponent entering Archie's law is between 1.3 and 1.5 for rocks showing damage evidenced by the presence of cracks. For intact samples, the cementation exponent is between 1.6 and 2.1. We have determined the value of the mobility of the counterions in the Stern layer (the inner part of the electrical DL coating the surface of the grains), and we found that this mobility is approximately 30 times smaller than in the bulk pore water in agreement with a recent work done on volcanic rocks.

APPENDIX A

NORMALIZED CHARGEABILITY: CONTROL BY THE STERN LAYER

In the context of the dynamic Stern layer model, the dependence of the surface conductivity with the frequency is purely related to the contribution of the Stern layer (Figure 3c)

$$\sigma'(\omega) = \frac{1}{F}\sigma_w + \sigma_S(\omega), \qquad (A\text{-}1)$$

where $\sigma_S(\omega)$ (in S m^{-1}) denotes a frequency-dependent surface conductivity. This conductivity has low- and high-frequency asymptotic values given by

$$\sigma_S^0 = \left(\frac{1}{F\phi}\right)\rho_g\beta_{(+)}(1-f)\text{CEC}, \qquad (A\text{-}2)$$

$$\sigma_S^\infty = \left(\frac{1}{F\phi}\right)\rho_g[\beta_{(+)}(1-f) + \beta_{(+)}^S f]\text{CEC}, \qquad (A\text{-}3)$$

respectively. In equation A-2, the DC surface conductivity is purely controlled by the diffuse layer. The contribution of the Stern layer is zero because the counterions remains stuck at the boundaries of the grains. At the opposite, at high frequencies, the contribution from the Stern and diffuse layers contribute to the surface conductivity. In the context of the linear conductivity model described by equation A-1, it is interesting to observe that the normalized chargeability is exactly the difference between the high-frequency surface conductivity and the low-frequency surface conductivity; i.e.

$$M_n \equiv \sigma_\infty - \sigma_0 = \sigma_S^\infty - \sigma_S^0, \qquad (A\text{-}4)$$

$$M_n = \left(\frac{1}{F\phi}\right)\rho_g\beta_{(+)}^S f\text{CEC}. \qquad (A\text{-}5)$$

APPENDIX B

SAND-CLAY MIXTURES

The goal of this appendix is to estimate the volume faction of clay in the smectite/sand mixes. We make the assumption that the mass density of the smectite particles (SWy-2-smectite from the Clay Mineralogical Society) is the same than the mass density of the sand grains (2650 kg m^{-3}, Ellis [1987]; in our case, we measured the mass density of totally dry smectite of 2670 kg m^{-3}). For clay minerals filling gradually the pore space between the sand grains, Revil et al. (2002) derive a formula connecting the volume fraction of clay φ_V to its weight fraction φ_W

$$\varphi_V = \left(\frac{\varphi_W}{1-\varphi_W}\right)\left(\frac{1-\phi_{Sd}}{1-\phi_{Cl}}\right), \qquad (B\text{-}1)$$

where ϕ_{Sd} and ϕ_{Cl} denote the porosity of the pure sand end member ($\phi_{Sd} \approx 0.52$; see Table 2) and the porosity of the pure smectite end member ($\phi_{Cl} \approx 0.90$; see Table 2), respectively. Equation B-1 is valid as long as $\varphi_V \leq \phi_{Sd}$; i.e., the clay particles are filling the space between the sand grains (shaly sand). For the Sd95 mix, we obtain $\varphi_V = 0.25$ and therefore approximately half of the pore space between the sand grains is occupied by very porous smectite. For the Sd90 mix, we obtain $\varphi_V = 0.53$ and therefore approximately all of the pore space between the sand grains is occupied by smectite. This is in agreement with a visual inspection of the mixture.

When the smectite entirely filled the space between the silica grains, the porosity and complex conductivity are given by $\phi = \phi_{Sd}\phi_{Cl}$ and $\sigma^* = (1/F_{Sd})\sigma_{Cl}^*$, where $F_{Sd} = \phi_{Sd}^{-1.5} \approx 2.7$. So it is not surprising that the spectra for the Sd95 and Sd90 are very similar to the spectra shown for pure smectite. From equation B-3, it implies that the phase for Sd90 should be the same as for pure smectite.

APPENDIX C

CONSTANT-PHASE MODEL

The complex resistivity $\rho^* = \rho' + i\rho''$ is related to the amplitude of the complex conductivity $\sigma^* = \sigma' + i\sigma''$ by $\rho^* = 1/\sigma^*$. The constant-phase model (also called Drake's complex resistivity model) is written as

$$\rho^*(\omega) = K(\omega_\rho + i\omega)^{-b}, \qquad (C\text{-}1)$$

where K is a constant and b is the positive exponent (generally $b \ll 1$, e.g., Börner, 1992) linearly related to the chargeability M and ω_ρ (>0) a characteristic frequency. From equation C-1,

$$\rho^*(\omega) = K \exp[-b \ln(\omega_\rho + i\omega)], \qquad (C\text{-}2)$$

$$\rho^*(\omega) = K \exp\left[-b \ln\sqrt{\omega_\rho^2 + \omega^2} - ib \tan^{-1}\left(\frac{\omega}{\omega_\rho}\right)\right], \qquad (C\text{-}3)$$

$$\rho^*(\omega) = K(\omega_\rho^2 + \omega^2)^{-\frac{b}{2}} \exp\left[-ib \tan^{-1}\left(\frac{\omega}{\omega_\rho}\right)\right]. \quad \text{(C-4)}$$

The complex resistivity can be expressed in terms of its amplitude and phase as

$$\rho^*(\omega) = |\rho^*(\omega)| \exp[i\varphi], \quad \text{(C-5)}$$

$$\rho = |\rho^*(\omega)| = K(\omega_\rho^2 + \omega^2)^{-\frac{b}{2}}, \quad \text{(C-6)}$$

$$\varphi = -b \tan^{-1}\left(\frac{\omega}{\omega_\rho}\right). \quad \text{(C-7)}$$

In the limit $\omega \gg \omega_\rho$, the phase is given by $b \approx -2\ \varphi/\pi$ and the amplitude by $\rho = K\omega^{-b}$. The FE between two frequencies ω and $A\omega$ is defined by

$$\text{FE} = \frac{\rho(\omega) - \rho(A\omega)}{\rho(\omega)}. \quad \text{(C-8)}$$

For small FEs (see Figure 17), equation C-8 is equivalent to equation 23 of the main text. From equation C-6, the FE between ω and $A\omega$ is given by FE $= 1 - A^b$ in the limit $\omega \gg \omega_\rho$. Using the expression $b \approx -2\ \varphi/\pi$ from equation C-7 in the same limit, we obtain

$$\text{FE} = 1 - A^{-\frac{2}{\pi}\varphi}, \quad \text{(C-9)}$$

$$\ln(1 - \text{FE}) = \ln A^{-\frac{2}{\pi}\varphi}. \quad \text{(C-10)}$$

Becaue FE $\ll 1$ (see Figure 17), we have

$$\text{FE} \approx -\frac{2}{\pi}\varphi \ln A, \quad \text{(C-11)}$$

which corresponds to equation 24 of the main text. Equation 25 is derived by multiplying the two sides of equation C-11 by the in-phase conductivity $\sigma'(A\omega)$ and using equation 22 for FE.

REFERENCES

Archie, G. E., 1942, The electrical resistivity log as an aid in determining some reservoir characteristics: Petroleum Transactions of AIME, **146**, 54–62, doi: 10.2118/942054-G.

Bolève, A., A. Crespy, A. Revil, F. Janod, and J. L. Mattiuzzo, 2007, Streaming potentials of granular media: Influence of the Dukhin and Reynolds numbers: Journal of Geophysical Research, **112**, B08204, doi: 10.1029/2006JB004673.

Börner, F. D., 1991, Untersuchungen zur komplexen elektrischen Leitfähigkeit von Gesteinen im Frequenzbereich von 1 Milliherz bis 10 Kiloherz: unpublished dissertation, Bergakademie Freiberg.

Börner, F. D., 1992, Complex conductivity measurements of reservoir properties: Proceedings of the Third European Core Analysis Symposium, 359–386.

Brunauer, S., P. H. Emmett, and E. Teller, 1938, Adsorption of gasses in multimolecular layers: Journal of the American Chemical Society, **60**, 309–319, doi: 10.1021/ja01269a023.

Bücker, M., and A. Hördt, 2013a, Long and short narrow pore models for membrane polarization: Geophysics, **78**, no. 6, E299–E314, doi: 10.1190/geo2012-0548.1.

Bücker, M., and A. Hördt, 2013b, Analytical modeling of membrane polarization with explicit parametrization of pore radii and the electrical double layer: Geophysical Journal International, **194**, 804–813, doi: 10.1093/gji/ggt136.

Chapman, H. D., 1965, Cation-exchange capacity, *in* C. A. Black, ed., Methods of soil analysis: Chemical and microbiological properties: Agronomy, **9**, 891–901.

Chapman, H. D., and P. F. Pratt, 1978, Methods of analysis for soils, plants, and waters: Division of Agricultural Sciences, 35–36.

Chelidze, T., and Y. Guéguen, 1999, Electrical spectroscopy of porous rocks: A review. I: Theoretical models: Geophysical Journal International, **137**, 1–15, doi: 10.1046/j.1365-246x.1999.00799.x.

Churcher, R. L., P. R. French, J. C. Shaw, and L. L. Schramm, 1991, Rock properties of Berea sandstone, Baker Dolomite and Indiana limestone: SPE Annual Technical Conference and Exhibition, SPE, 431–446, doi: 10.2118/21044-MS.

Cole, K. S., and R. H. Cole, 1941, Dispersion and absorption in dielectrics. I: Alternating current characteristics: Journal of Chemical Physics, **9**, 341–351, doi: 10.1063/1.1750906.

Comparon, L., 2005, Etude expérimentale des propriétés électriques et diélectriques des matériaux argileux consolidés: Ph.D. thesis, Institut de Physique du Globe de Paris.

Cremers, A., 1968, Surface conductivity in sodium clays: Israel Journal of Chemistry, **6**, 195–202, doi: 10.1002/ijch.v6.3.

Davydycheva, S., N. Rykhlinski, and P. Legeido, 2006, Electrical prospecting method for oil search using the induced polarization effect: Geophysics, **71**, no. 4, G179–G189, doi: 10.1190/1.2217367.

Dukhin, S. S., and V. N. Shilov, 1974, Dielectrical phenomena and the double layer in disperse systems and polyelectrolytes: Wiley.

Ellis, D. V., 1987, Well logging for earth scientists: Elsevier Science, 527.

Fixman, M., 1980, Charged macromolecules in external fields. I: The sphere: Journal of Chemical Physics, **72**, 5177–5186, doi: 10.1063/1.439753.

Godelitsas, A., P. Gamaletsos, and M. R. Kotsis, 2010, Mordenite-bearing tuffs from Prassa quarry, Kimolos island, Greece: European Journal of Mineralogy, **22**, 797–811, doi: 10.1127/0935-1221/2010/0022-2058.

Gouy, G. L., 1910, Sur la constitution de la charge électrique à la surface d'un électrolyte: Journal de Physique Théorique et Appliquée, **9**, 457–468, doi: 10.1051/jphystap:019100090045700.

Grosse, C., 2009, Generalization of a classic theory of the low frequency dielectric dispersion of colloidal suspensions to electrolyte solutions with different ion valences: Journal of Physical Chemistry B, **113**, 11201–11215, doi: 10.1021/jp904742v.

Grosse, C., and V. N. Shilov, 2000, Conductivity, permittivity, and characteristic time of colloidal suspensions in weak electrolyte solutions: Journal of Colloid and Interface Science, **225**, 340–348, doi: 10.1006/jcis.2000.6750.

Kemna, A., A. Binley, and L. D. Slater, 2004, Crosshole IP imaging for engineering and environmental applications: Geophysics, **69**, 97–107, doi: 10.1190/1.1649379.

Kurniawan, B., 2005, Shaly sand interpretation using CEC-dependent petrophysical parameters: Ph.D. thesis, Louisiana State University.

Leroy, P., and A. Revil, 2009, A mechanistic model for the spectral induced polarization of clay materials: Journal of Geophysical Research, **114**, B10202, doi: 10.1029/2008JB006114.

Leroy, P., A. Revil, A. Kemna, P. Cosenza, and A. Ghorbani, 2008, Complex conductivity of water-saturated packs of glass beads: Journal of Colloid and Interface Science, **321**, 103–117, doi: 10.1016/j.jcis.2007.12.031.

Lira, B. P., A. O. Polo, E. M. O. Sánchez, E. R. Ruiz, O. A. A. Sandoval, F. P. García, and C. A. G. Ramírez, 2013, Physical characterization of an extensive volcanic rock in México: "Red tezontle" from Cerro de la Cruz, in Tlahuelilpan, Hidalgo: Acta Universitaria, **23**, 9–15.

Lorne, B., F. Perrier, and J.-P. Avouac, 1999, Streaming potential measurements. 1: Properties of the electrical double layer from crushed rock samples: Journal of Geophysical Research, **104**, 857–877, doi: 10.1029/1999JB900156.

Lowell, S., and J. E. Shields, 1979, Powder surface area and porosity, 2nd ed.: Chapman and Hall, 1–234.

Mansoor, N., and L. Slater, 2007, On the relationship between iron concentration and induced polarization in marsh soils: Geophysics, **72**, no. 1, A1–A5, doi: 10.1190/1.2374853.

Mao, D., A. Revil, and J. Hinton, 2016, Induced polarization response of porous media with metallic particles. Part 4: Detection of metallic and non-metallic targets in time domain induced polarization tomography: Geophysics, **81**, no. 4, D359–D375, doi: 10.1190/geo2015-0480.1.

Marshall, D. J., and T. R. Madden, 1959, Induced polarization, a study of its causes: Geophysics, **24**, 790–816, doi: 10.1190/1.1438659.

Niu, Q., M. Prasad, A. Revil, and M. Saidian, 2016a, Textural control on the quadrature conductivity of porous media: Geophysics, **81**, no. 5, E297–E309, doi: 10.1190/geo2015-0715.1.

Niu, Q., and A. Revil, 2016, Connecting complex conductivity spectra to mercury porosimetry of sedimentary rocks: Geophysics, **81**, no. 1, E17–E32, doi: 10.1190/geo2015-0072.1.

Niu, Q., A. Revil, and M. Saidian, 2016b, Salinity dependence of the complex surface conductivity of the Portland sandstone: Geophysics, **81**, no. 2, D125–D140, doi: 10.1190/geo2015-0426.1.

Olhoeft, G. R., 1985, Low-frequency electrical properties: Geophysics, **50**, 2492–2503, doi: 10.1190/1.1441880.

Pelton, W. H., S. H. Ward, P. G. Hallof, W. R. Sill, and P. H. Nelson, 1978, Mineral discrimination and removal of inductive coupling with multifrequency IP: Geophysics, **43**, 588–609, doi: 10.1190/1.1440839.

Revil, A., 1999, Ionic diffusivity, electrical conductivity, membrane and thermoelectric potentials in colloids and granular porous media: A unified model: Journal of Colloid and Interface Science, **212**, 503–522, doi: 10.1006/jcis.1998.6077.

Revil, A., 2012, Spectral induced polarization of shaly sands: Influence of the electrical double layer: Water Resources Research, **48**, W02517, doi: 10.1029/2011WR011260.

Revil, A., 2013a, Effective conductivity and permittivity of unsaturated porous materials in the frequency range 1 mHz–1GHz: Water Resources Research, **49**, 306–327, doi: 10.1029/2012WR012700.

Revil, A., 2013b, On charge accumulations in heterogeneous porous materials under the influence of an electrical field: Geophysics, **78**, no. 4, D271–D291, doi: 10.1190/GEO2012-0503.1.

Revil, A., A. Binley, L. Mejus, and P. Kessouri, 2015, Predicting permeability from the characteristic relaxation time and intrinsic formation factor of complex conductivity spectra: Water Resources Research, **51**, 6672–6700, doi: 10.1002/2015WR017074.

Revil, A., A. Coperey, Z. Shao, N. Florsch, I. L. Fabricius, Y. Deng, J. R. Delsman, P. S. Pauw, M. Karaoulis, P. G. B. de Louw, E. S. van Baaren, W. Dabekaussen, A. Menkovic, and J. L. Gunnink, 2017c, Complex conductivity of soils: Water Resources Research, **53**, 7121–7147, doi: 10.1002/wrcr.v53.8.

Revil, A., J. D. Eppehimer, M. Skold, M. Karaoulis, L. Godinez, and M. Prasad, 2013a, Low-frequency complex conductivity of sandy and clayey materials: Journal of Colloid and Interface Science, **398**, 193–209, doi: 10.1016/j.jcis.2013.01.015.

Revil, A., and N. Florsch, 2010, Determination of permeability from spectral induced polarization data in granular media: Geophysical Journal International, **181**, 1480–1498, doi: 10.1111/j.1365-246X.2010.04573.x.

Revil, A., N. Florsch, and C. Camerlynck, 2014a, Spectral induced polarization porosimetry: Geophysical Journal International, **198**, 1016–1033, doi: 10.1093/gji/ggu180.

Revil, A., D. Grauls, and O. Brévart, 2002, Mechanical compaction of sand/clay mixtures: Journal of Geophysical Research, **107**, ECV 11-1–ECV 11-15, doi: 10.1029/2001JB000318.

Revil, A., P. Kessouri, and C. Torres-Verdín, 2014b, Electrical conductivity, induced polarization, and permeability of the Fontainebleau sandstone: Geophysics, **79**, no. 5, D301–D318, doi: 10.1190/geo2014-0036.1.

Revil, A., M. Le Breton, Q. Niu, E. Wallin, E. Haskins, and D. M. Thomas, 2017a, Induced polarization of volcanic rocks. 1: Surface versus quadrature conductivity: Geophysical Journal International, **208**, 826–844, doi: 10.1093/gji/ggw444.

Revil, A., M. Le Breton, Q. Niu, E. Wallin, E. Haskins, and D. M. Thomas, 2017b, Induced polarization of volcanic rocks. 2: Influence of pore size and permeability: Geophysical Journal International, **208**, 814–825, doi: 10.1093/gji/ggw382.

Revil, A., W. F. Woodruff, C. Torres-Verdín, and M. Prasad, 2013b, Complex conductivity tensor of hydrocarbon-bearing shales and mudrocks: Geophysics, **78**, no. 6, D403–D418, doi: 10.1190/geo2013-0100.1.

Rosen, L. A., and D. A. Saville, 1991, Dielectrical spectroscopy of colloidal dispersions: Comparisons between experiment and theory: Langmuir, **7**, 36–42, doi: 10.1021/la00049a009.

Schlumberger, C., 1920, Study of underground electrical prospecting: Paris, 99.

Schmutz, M., A. Blondel, and A. Revil, 2012, Saturation dependence of the quadrature conductivity of oil-bearing sands: Geophysical Research Letters, **39**, L03402, doi: 10.1029/2011GL050474.

Schmutz, M., A. Revil, P. Vaudelet, M. Batzle, P. Femenía Viñao, and D. D. Werkema, 2010, Influence of oil saturation upon spectral induced polarization of oil bearing sands: Geophysical Journal International, **183**, 211–224, doi: 10.1111/j.1365-246X.2010.04751.x.

Sen, P. N., and P. A. Goode, 1992, Influence of temperature on electrical conductivity on shaly sands: Geophysics, **57**, 89–96, doi: 10.1190/1.1443191.

Sen, P. N., C. Scala, and M. H. Cohen, 1981, Self-similar model for sedimentary rocks with application to the dielectric constant of fused glass beads: Geophysics, **46**, 781–795, doi: 10.1190/1.1441215.

Shinzato, M. C., T. J. Montanheiro, V. A. Janasi, S. Andrade, and J. K. Yamamoto, 2012, Removal of Pb2+ from aqueous solutions using two Brazilian rocks containing zeolites: Environmental Earth Sciences, **66**, 363–370, doi: 10.1007/s12665-011-1245-z.

Shuey, R. T., and M. Johnson, 1973, On the phenomenology of electrical relaxation in rocks: Geophysics, **38**, 37–48, doi: 10.1190/1.1440331.

Tarasov, K., and K. Titov, 2013, On the use of the Cole-Cole equations in spectral induced polarization: Geophysical Journal International, **195**, 352–356, doi: 10.1093/gji/ggt251.

Titov, K., A. Tarasov, Y. Ilyin, N. Seleznev, and A. Boyd, 2010, Relationships between induced polarization relaxation time and hydraulic properties of sandstone: Geophysical Journal International, **180**, 1095–1106, doi: 10.1111/j.1365-246X.2009.04465.x.

Van Voorhis, G. D., P. H. Nelson, and T. L. Drake, 1973, Complex resistivity spectra of porphyry copper mineralization: Geophysics, **38**, 49–60, doi: 10.1190/1.1440333.

Vaudelet, P., A. Revil, M. Schmutz, M. Franceschi, and P. Bégassat, 2011a, Induced polarization signature of the presence of copper in saturated sands: Water Resources Research, **47**, W02526, doi: 10.1029/2010WR009310.

Vaudelet, P., A. Revil, M. Schmutz, M. Franceschi, and P. Bégassat, 2011b, Changes in induced polarization associated with the sorption of sodium, lead, and zinc on silica sands: Journal of Colloid and Interface Science, **360**, 739–752, doi: 10.1016/j.jcis.2011.04.077.

Vinegar, H. J., and M. H. Waxman, 1984, Induced polarization of shaly sands: Geophysics, **49**, 1267–1287, doi: 10.1190/1.1441755.

Waxman, M. H., and L. J. M. Smits, 1968, Electrical conductivities in oil bearing shaly sands: SPE Journal, **8**, 107–122, doi: 10.2118/1863-A.

Weller, A., L. Slater, and S. Nordsiek, 2013, On the relationship between induced polarization and surface conductivity: Implications for petrophysical interpretation of electrical measurements: Geophysics, **78**, no. 5, D315–D325, doi: 10.1190/geo2013-0076.1.

Woodruff, W. F., A. Revil, and C. Torres-Verdín, 2014, Laboratory determination of the complex conductivity tensor of unconventional anisotropic shales: Geophysics, **79**, no. 5, E183–E200, doi: 10.1190/geo2013-0367.1.

Zimmermann, E., A. Kemna, J. Berwix, W. Glaas, H. Munch, and J. Huisman, 2008, A high-accuracy impedance spectrometer for measuring sediments with low polarizability: Measurement Science and Technology, **19**, 105603, doi: 10.1088/0957-0233/19/10/105603.

Zisser, N., A. Kemna, and G. Nover, 2010, Relationship between low-frequency electrical properties and hydraulic permeability of low-permeability sandstones: Geophysics, **75**, no. 3, E131–E141, doi: 10.1190/1.3413260.

Zisser, N., and G. Nover, 2009, Anisotropy of permeability and complex resistivity of tight sandstones subjected to hydrostatic pressure: Journal of Applied Geophysics, **68**, 356–370, doi: 10.1016/j.jappgeo.2009.02.010.

Zukoski, C. F., and D. A. Saville, 1986a, The interpretation of electrokinetic measurements using a dynamic model of the Stern layer. I: The dynamic model: Journal of Colloid and Interface Science, **114**, 32–44, doi: 10.1016/0021-9797(86)90238-9.

Zukoski, C. F., and D. A. Saville, 1986b, The interpretation of electrokinetic measurements using a dynamic model of the Stern layer. II: Comparisons between theory and experiments: Journal of Colloid and Interface Science, **114**, 45–53, doi: 10.1016/0021-9797(86)90239-0.